

Reconstruction of stochastic 3-D signals with symmetric statistics from 2-D projection images motivated by cryo-electron microscopy

Nan Xu, *Member, IEEE* and Peter C. Doerschuk, *Senior Member, IEEE*

Abstract—Cryo-electron microscopy provides 2-D projection images of the 3-D electron scattering intensity of many instances of the particle under study (e.g., a virus). Both symmetry (rotational point groups) and heterogeneity are important aspects of biological particles and both aspects can be combined by describing the electron scattering intensity of the particle as a stochastic process with a symmetric probability law and therefore symmetric moments. A maximum likelihood estimator implemented by an expectation-maximization algorithm is described which estimates the unknown statistics of the electron scattering intensity stochastic process from images of instances of the particle. The algorithm is demonstrated on the bacteriophage HK97 and the virus N ω V. The results are contrasted with existing algorithms which assume that each instance of the particle has the symmetry rather than the less restrictive assumption that the probability law has the symmetry.

Index Terms—cryo-electron microscopy, viruses, symmetric statistics, maximum likelihood reconstruction, heterogeneity characterization

I. INTRODUCTION

STRUCTURAL BIOLOGY is the study of the 3-D geometry of biological particles such as viruses, ribosomes, enzymes, *etc.* The 3-D geometry, typically called the “structure,” can be as detailed as the 3-D location of each atom in the particle or, if only lower resolution is achievable, the electron scattering intensity as a function of position in 3-D. Understanding the 3-D geometry of synthetic nanoparticles is also becoming important in materials science [1].

Single-particle cryo-electron microscopy (cryo-EM) [2] is an experimental method for structure determination which is of great and increasing importance [3] and which has been recognized with the 2017 Nobel Prize in Chemistry [4]. In this method, many instances of the particle are flash frozen to the temperature of liquid nitrogen. Images with pixel dimensions of about 1 Å are recorded. Each image shows many instances of the particle. No instance of the particle is imaged more than once in order to minimize damage to the instance of the particle from the electron beam of the microscope. The many images (typically 10^4 – 10^6), each a projection image with an unknown projection direction, are computationally combined

to yield one 3-D reconstruction of the electron scattering intensity of the particle. In favorable situations, nearly atomic resolution (e.g., 2–3 Å) spatial resolution can be achieved in the 3-D reconstruction of the electron scattering intensity. This paper describes an integrated approach to two aspects of this reconstruction problem: heterogeneity among the particles and symmetry of the particles.

Alternative techniques involving electron microscopy include electron crystallography (based on 2-D crystals) and electron cryotomography (based on recording images of a single specimen at a variety of tilt positions of the microscope’s stage, generally limited to approximately $\pm 70^\circ$ of tilt) [5]. The idea of symmetry constraints on the statistics of the electron scattering intensity, which is central to this paper, could be applied to these alternative methods. However, the estimation problem relating the data and the electron scattering intensity would be different for each of these alternative methods.

A. Heterogeneity

Instances of a particle can differ, i.e., the particles are heterogeneous. Two mechanisms by which heterogeneity can occur are compositional differences and flexibility. An eukaryotic 80S ribosome can be an example of a particle with compositional differences. Such a ribosome (i) has a molecular mass of about 3.2×10^6 Dalton, (ii) has dimensions of 250–300 Å, and (iii) is composed of about 80 protein molecules plus about 4 RNA molecules. The ribosome’s function is to assemble on the mRNA that will be translated into the corresponding protein molecule and catalyze the translation. Such a ribosome has been reported to have compositional variability [6] and such variability is one source of heterogeneity.

Flexibility is a second source of heterogeneity, as is indicated by the fact that the protein structures obtained from X-ray crystallography experiments do not always show the entire protein amino acid sequence (which is separately known from molecular biology methods) but rather lacks certain disordered portions of the molecule. When heterogeneity is due to particle motions, at least large-space long-time characteristics of the motion are preserved in the frozen specimen that is imaged because the freezing to the temperature of liquid nitrogen is fast (10^6 °C/sec with vitrification occurring in 10^{-4} sec [7]).

As is described in the second paragraph of Section I, the image shows many instances of the particle. Subimages showing individual instances are extracted and used for further processing. This extraction process has errors which complicate characterizing the heterogeneity of the instances.

N. Xu was with the School of Electrical and Computer Engineering, Cornell University, Ithaca, NY, 14853 USA. She is now with the Wallace H. Coulter Department of Biomedical Engineering, Georgia Institute of Technology and Emory University, Atlanta, Georgia 30332, USA e-mail: im.nan.xu@gmail.com

P. C. Doerschuk is with the School of Electrical and Computer Engineering and the Meinig School of Biomedical Engineering, Cornell University, Ithaca, NY, 14853 USA e-mail: pd83@cornell.edu

When all instances of the particle are identical, standard software (e.g., Refs. [8]–[10]) can typically compute a structure. When each instance of the particle comes from one of a few number of classes (typically less than ten) and all instances in a class are identical (described as discrete heterogeneity), standard software (e.g., Refs. [8]–[10]) can often compute a structure for each class.

The case when the instances in a class differ (described as continuous heterogeneity) has been described as an important issue in multiple review articles over a range of years, e.g., [11, p. 221] to [12, p. 55] to the report of the 2017 Nobel Prize in Chemistry [4]. Describing the heterogeneity of the instances of a particle by a mixture density with a finite number of classes [13] is a combination of discrete and continuous heterogeneity. If only a single class is used then the continuous heterogeneity might describe large scale variability among the instances of the particle. Alternatively, if a finite set of classes is used then the changes among the instances within a class might be smaller. Multiple statements of this problem exist and multiple algorithms exist which address the solution of the different problem statements [14]. The problem statement addressed in this paper is (1) to characterize continuous heterogeneity within a class directly from the image data without additional information, (2) to provide a statistical characterization that is relevant for smaller-scale fluctuations that would occur within a class, and (3) to apply symmetry constraints to the statistics rather than to the individual instances.

Alternative problem statements focus on one or more issues including the following issues:

- Use additional information: For instance, Refs. [15], [16] start with a reference structure from which normal modes can be computed and then compare projections of the reference structure deformed by the normal modes with the images.
- Large-scale motions: For instance, Refs. [17], [18] is a manifold-based method for interpolating among the many structures that can be computed from certain datasets such as the ribosome dataset of Ref. [17].
- Compute properties of the continuously heterogeneous particle ensemble: For instance, Ref. [19] computes, directly from image data, the first few (e.g., 5) principal values and components of the 3-D electron scattering intensity of the particle.

Many problem statements and algorithm solutions, some of which are described above, have been recently reviewed [14]. Additional recent reviews [20], [21] by the primary authors of two of the widely used software systems describe fewer problem statements and algorithm solutions. For instance, Ref. [20] describes only methods for dealing with discrete heterogeneity and Ref. [21] describes only methods for dealing with discrete heterogeneity with some extensions to some forms of continuous heterogeneity when subregions of the structure move as rigid bodies [21, Sections 4.4–4.6]. Therefore, new methods for characterizing continuous heterogeneity are needed.

Data resampling [22]–[26] is one class of existing approaches: multiple datasets are created by resampling the

original dataset, a structure is computed for each dataset, and then statistics are computed by averaging over the multiple structures. When the particle has symmetry, the symmetry is generally imposed on each of the structures. This may be the reason that the resulting spatial variance functions (i.e., the variance as a function of position) are known to have anomalous peaks on and near symmetry axes of the particle [20, p. 173]. Since the symmetry axes can be the location of important biology, e.g., the Flock House Virus example of Section I-B, anomalous results near symmetry axes is not a satisfactory situation. However, computing asymmetry reconstructions and allowing the symmetry to appear in the averaging operation requires substantially more data and computation and may not be practical.

In order to describe a second class of approaches, based on moments [27]–[30], it is helpful to describe the mathematical description of the image that is used. Different methods describe the instance of the particle using different mathematics, for instance, a 3-D array of voxel values [9], a truncated 3-D Fourier series [31], or a weighted sum of basis functions where the basis functions are chosen in order to achieve sparse matrix operations [29]. The voxel values, Fourier series coefficients, or weights for the i th particle (or, equivalently, the i th image since each particle is imaged only once) are packed into a vector which is denoted by c_i . The i th image, denoted by y_i , is a linear transformation of c_i plus an additive noise, denoted by w_i . The transformation, denoted by L , includes physical processes such as the 3-D to 2-D projection and the Contrast Transfer Function (CTF) of the microscope. The transformation L contains parameters, e.g., the direction of the 3-D to 2-D projection, which vary from particle to particle and these parameters are denoted by θ_i . Therefore, $y_i = L(\theta_i)c_i + w_i$. The collections $\{\theta_i\}_{i=1}^{N_v}$, $\{c_i\}_{i=1}^{N_v}$, $\{w_i\}_{i=1}^{N_v}$ are independent and the θ_i , c_i (mean \bar{c} , covariance \mathbf{V}), and w_i (mean 0, covariance \mathbf{Q}) are all i.i.d. Therefore, conditional on the value of θ_i , the mean and covariance of y is $\bar{y} = L(\theta_i)\bar{c}$ and $\Sigma = L(\theta_i)\mathbf{V}L^T(\theta_i) + \mathbf{Q}$, respectively. Idealizations in the mathematical model include the fact that multiple noise sources are present and the CTF of the microscope effects some of the noise sources, the noise is not purely additive, and the noise is not independent of the signal.

Having described the mathematical model, we can describe the second class of approaches which are based on moments [27]–[30]. The basic idea of the moment estimators is to estimate Σ by a sample covariance and then estimate \mathbf{V} from the covariance equation which is linear in \mathbf{V} . All methods must assume that the values of θ_i , which are estimated from the data, are correct. Additionally, if the instances of the particle come from multiple classes of particle, the estimate of the class must also be correct. Resolution is limited in some methods, e.g., $16 \times 16 \times 16$ voxels [27]. In some methods [29], [32], the solution of the linear system is done in a basis where the system is sparse thereby enabling the solution of large problems, e.g., $10^3 \times 10^3$. Estimation of θ_i would probably be done in the context of assuming that the covariance \mathbf{V} is zero. Ref. [33, Supplemental Figure 1] provides some numerical results on the extent to which estimates of θ_i change

when the covariance \mathbf{V} is simultaneously estimated. In the particular case of Ref. [33], about 10% of the particles changed orientation, including 5% with large orientation changes.

Using a model similar to the model of the previous paragraph, the mean and covariance of the random vectors c_i can be estimated for each class by a third approach which uses a maximum likelihood estimator computed by an expectation-maximization algorithm in which θ_i are the nuisance parameters [33]–[39]. The present paper is an extension of these ideas, which are described in more detail in Section II.

The biological analysis is typically based on the variance function. In more detail, let the electron scattering stochastic process be denoted by $\rho(\mathbf{x}) \in \mathbb{R}^1$ where $\mathbf{x} \in \mathbb{R}^3$ and expectation be denoted by E . Then the mean function is $\bar{\rho}(\mathbf{x}) = E[\rho(\mathbf{x})]$, the covariance function is $C(\mathbf{x}_1, \mathbf{x}_2) = E[(\rho(\mathbf{x}_1) - \bar{\rho}(\mathbf{x}_1))(\rho(\mathbf{x}_2) - \bar{\rho}(\mathbf{x}_2))]$, the variance function is $v(\mathbf{x}) = C(\mathbf{x}, \mathbf{x})$, and the standard deviation function is $s(\mathbf{x}) = \sqrt{v(\mathbf{x})}$ which is usefully primarily because it has the same units as $\rho(\mathbf{x})$. Focusing on the variance function, which is the common choice, clearly ignores a great deal of critically important information since $C(\mathbf{x}_1, \mathbf{x}_2)$ contains information on how the electron density behaves at spatially separated locations, but that information is missing from $v(\mathbf{x})$. To the best of our knowledge, this is the first publication in which a complete 6-D covariance ($C(\mathbf{x}_1, \mathbf{x}_2)$) analysis is performed for particles with symmetry. In the numerical examples of Section VIII the covariance matrix \mathbf{V} that determines $C(\mathbf{x}_1, \mathbf{x}_2)$ is assumed to be diagonal in order to decrease the amount of computation but all the formulas in the paper apply for arbitrary \mathbf{V} .

B. Symmetry

An important characteristic of many systems is symmetry, i.e., the electron scattering intensity is invariant under the operations of a symmetry group. On 05 November 2017, the Protein Data Bank [40] contained 130,005 structures in seven symmetry classes: Asymmetric (60.198%), Cyclic C_n (31.020% with n ranging from 2 to 39 [41], [42]), Dihedral D_n (7.517% with n ranging from 2 to 48 [43]), Icosahedral I (0.491%), Tetrahedral T (0.280%), Octahedral O (0.248%), and Helical (0.245%). We focus on the rotational point groups, which are I , O , T , C_n , and D_n , and which have 60, 24, 12, n , and $2n$ symmetry operations, respectively. Helical is a line group.

Many viruses have a protein shell that surrounds the genome of the virus and the shell has icosahedral symmetry [44]. The most compelling evidence for the existence of such symmetries is atomic-resolution x-ray crystallography. In particular, the particle has sufficiently small compositional heterogeneity and flexibility heterogeneity to form a crystal; the non-physiological particle-particle contacts in the crystal further reduce heterogeneity; high-resolution (e.g., 2.0–3.0 Å) x-ray diffraction data is recorded; the data is analyzed under the assumption of icosahedral symmetry; and the resulting atomic positions agree with chemical (e.g., bond lengths), biochemical (e.g., left-handed amino acids), and molecular biology (e.g., sequence of amino acids) knowledge about the particle which is the evidence that the icosahedral symmetry assumption

used in the analysis of the data is correct. But even particles with atomic-resolution x-ray crystallographic structures are not rigid. For instance, Flock House Virus has such a structure, the pentamer of γ peptides near the 5-fold symmetry axis of the icosahedrally symmetric particle appear on the interior surface of the capsid in the atomic-resolution structure [45], [46], but biochemical and cell biological evidence indicates that the pentamer is sometimes on the surface of the particle and plays a role in the entry of the particle into a new host cell [47], [48].

In this paper, we assume that the correct symmetry is known. If there is uncertainty in the symmetry, then multiple calculations can be performed, each with a different symmetry, and the results (including the value of the likelihood function and whether the answer makes sense to the biologist) can be employed to determine the correct symmetry.

C. Combining symmetry and heterogeneity and outline of the paper

In this paper we combine ideas of symmetry and continuous heterogeneity by applying the symmetry to the statistics of the particle. This implies (Section III) that the moments of the electron scattering intensity satisfy constraints. Our numerical results appear to indicate that this approach avoids introducing anomalous peaks in the variance function ($v(\mathbf{x})$) on and near symmetry axes of the particle which occur with standard resampling methods of estimating the variance function [20, p. 173], as was described in Section I-A.

Details of the symmetry groups influence the organization of the paper. In particular, if all the irreducible representations [49, Theorem 3.3 p. 69] (see also paragraph 3 of Section IV) (irreps) of the group are real, then there are suitable real-valued basis functions so that an orthonormal expansion of the real-valued electron scattering intensity can be determined with real-valued coefficients. Real irreps are possible for the icosahedral group, which is the symmetry group of our example virus reconstruction problems, and so the main body of the paper focuses on that simpler case while the case where real irreps are not possible, which includes important cases such as cyclic symmetry, is described in Appendix D.

The choice of the coordinate system in \mathbb{R}^3 that is used to describe the particle also influences the organization of the paper. Particles exhibiting I , O , or T symmetries are likely to be most parsimoniously described in spherical coordinates but particles exhibiting C_n or D_n may be better described in cylindrical coordinates. Since our example has icosahedral (I) symmetry, the main body of the paper focuses on spherical coordinates while the case of cylindrical coordinates is described in Appendix E.

The reminder of the paper is organized as follows. The maximum likelihood estimator approach [34] that is generalized in this paper with a new signal model is described in Section II. The new signal model is described in parts: symmetry (Section III), basis functions respecting the symmetry (Section IV) and constraints on the linear combinations of basis functions needed to achieve symmetric statistics

(Section V and Appendices A, B, and C). The changes needed in the maximum likelihood estimator in order to use the new signal model are described in Section VI. Numerical results on simulated and experimental data are described in Section VIII and conclusions in Section IX.

D. Notation

- 1) “Probability density function” (“probability mass function”) is abbreviated by “pdf” (“pmf”).
- 2) The multivariable Gaussian pdf with mean μ and covariance Σ evaluated at y is denoted by $N(\mu, \Sigma)(y)$.
- 3) E denotes expectation.
- 4) i.i.d. stands for “independent and identically distributed.”
- 5) $\mathbf{x} \in \mathbb{R}^3$ and $x = \|\mathbf{x}\|_2$.
- 6) The quantity \mathbf{x}/x is a unit vector and, since $\mathbf{x} \in \mathbb{R}^3$, is shorthand for the two angles of spherical coordinates.
- 7) Superscript $*$ is complex conjugation.
- 8) I_n is the $n \times n$ identity matrix and $0_{m,n}$ is the $m \times n$ zero matrix.
- 9) $\int d\Omega$ is integration over the surface of the sphere in 3-D, which, in spherical coordinates, is $\int_{\theta=0}^{\pi} \int_{\phi=0}^{2\pi} \sin(\theta) d\theta d\phi$. If $\mathbf{x} \in \mathbb{R}^3$ is described in spherical coordinates as $\mathbf{x} = (x, \theta, \phi)$ and f is a function of \mathbf{x} then $\int f(\mathbf{x}) d\Omega$ is a function of x , i.e., the integral is over the surface of a sphere at radius x .
- 10) The Kronecker delta function $\delta_{m,n}$ is defined by $\delta_{m,n} = 1$ if $m = n$, and $\delta_{m,n} = 0$ otherwise, where m and n are integers or vectors of integers.

II. MAXIMUM LIKELIHOOD RECONSTRUCTION

Because this paper extends Ref. [34], in this section we summarize Ref. [34] for the special case where all the particles that are imaged come from the same class and where the pdf on the projection orientations is known. We describe the problem in the context of cryo-EM, but any application having a linear imaging equation containing nuisance parameters would share the equations.

The electron scattering intensity $\rho(\mathbf{x})$ is described as a linear superposition of known basis functions $F_\omega(\mathbf{x})$ with weights c_ω :

$$\rho(\mathbf{x}) = \sum_{\omega \in \Omega} c_\omega F_\omega(\mathbf{x}). \quad (1)$$

The goal of the reconstruction is to estimate the joint pdf on the c_ω .

The imaging process is linear from $\rho(\mathbf{x})$ to image and therefore also from c_ω to image, with unknown nuisance parameters in the linear transformation, and has additive noise. Let \mathbf{y}_i be the i th image. Let \mathbf{c}_i be the vector of c_ω for the i th image. Let z_i be the nuisance parameters for the i th image and $\mathbf{L}(z_i)$ be the linear transformation [50]–[53]. Let \mathbf{w}_i be the noise. Then [34, Eq. 3],

$$\mathbf{y}_i = \mathbf{L}(z_i) \mathbf{c}_i + \mathbf{w}_i. \quad (2)$$

The random variables z_i , \mathbf{c}_i , \mathbf{w}_i ($i \in \{1, \dots, N_v\}$) are independent and z_i is uniform on rotations, $\mathbf{c}_i \sim N(\bar{\mathbf{c}}, \mathbf{V})$, and $\mathbf{w}_i \sim N(\mathbf{0}, \mathbf{Q})$.

The maximum likelihood estimator (MLE) of $\bar{\mathbf{c}}$ and \mathbf{V} is computed by a generalized expectation-maximization (E-M) algorithm using the z_i as nuisance variables. The update equation for the new value of $\bar{\mathbf{c}}$ is [34, Eq. 33] $\mathbf{F}\bar{\mathbf{c}}^{\text{new}} = \mathbf{g}$ where

$$\mathbf{F} = \sum_{i=1}^{N_v} \int_{z_i} \mathbf{L}^T(z_i) \Sigma_i^{-1}(z_i, \mathbf{V}_0) \mathbf{L}(z_i) p(z_i | \mathbf{y}_i, \bar{\mathbf{c}}_0, \mathbf{V}_0) dz_i \quad (3)$$

$$\mathbf{g} = \sum_{i=1}^{N_v} \int_{z_i} \mathbf{L}^T(z_i) \Sigma_i^{-1}(z_i, \mathbf{V}_0) \mathbf{y}_i p(z_i | \mathbf{y}_i, \bar{\mathbf{c}}_0, \mathbf{V}_0) dz_i, \quad (4)$$

subscript “0” indicates the previous value, $\Sigma_i(z_i, \mathbf{V}) = \mathbf{L}(z_i) \mathbf{V} \mathbf{L}^T(z_i) + \mathbf{Q}$ [34, Eq. 7], $p(z_i | \mathbf{y}_i, \bar{\mathbf{c}}, \mathbf{V})$ is computed from $p(\mathbf{y}_i | z_i, \bar{\mathbf{c}}, \mathbf{V}) = N(\boldsymbol{\mu}_i(z_i, \bar{\mathbf{c}}), \Sigma_i(z_i, \mathbf{V}))(\mathbf{y}_i)$ [34, Eq. 8], and $\boldsymbol{\mu}_i(z_i, \bar{\mathbf{c}}) = \mathbf{L}(z_i) \bar{\mathbf{c}}$ [34, Eq. 5]. The update equation for the new value of \mathbf{V} is to solve the maximization problem [34, Eq. 35] $\mathbf{V}^{\text{new}} = \arg \max_{\mathbf{V}} Q(\mathbf{V})$ where

$$Q(\mathbf{V}) = \sum_{i=1}^{N_v} \int_{z_i} \ln \det(\Sigma_i^{-1}(z_i, \mathbf{V}_0)) p(z_i | \mathbf{y}_i, \bar{\mathbf{c}}_0, \mathbf{V}_0) dz_i$$

$$- \sum_{i=1}^{N_v} \int_{z_i} \text{tr}[\Sigma_i^{-1}(z_i, \mathbf{V}_0) \mathbf{N}_i(\mathbf{y}_i, z_i, \bar{\mathbf{c}}_0)] p(z_i | \mathbf{y}_i, \bar{\mathbf{c}}_0, \mathbf{V}_0) dz_i \quad (5)$$

and $\mathbf{N}_i(\mathbf{y}_i, z_i, \bar{\mathbf{c}}) = (\mathbf{y}_i - \boldsymbol{\mu}_i(z_i, \bar{\mathbf{c}}))(\mathbf{y}_i - \boldsymbol{\mu}_i(z_i, \bar{\mathbf{c}}))^T$ [34, Eq. 34], which is solved by MATLAB’s `fmincon` (option “trust-region-reflective”) with symbolic cost, gradient of the cost, and Hessian of the cost. Any set of basis functions $F_\omega(\mathbf{x})$ could be used within $\mathbf{L}(z_i)$ and the only constraint is that \mathbf{V} is positive definite.

The estimator of Ref. [34] has two capabilities that are not described in this paper: (i) If the collection of cryo-EM images are unlabeled images from a known number of classes, the *a priori* pmf for class membership is estimated and a separate value of $\bar{\mathbf{c}}$ and \mathbf{V} is estimated for each class. (ii) If desired, the uniform *a priori* pdf/pmf on the nuisance parameters, such as the projection orientations, can be replaced by an unknown pdf/pmf that is estimated. The treatment of symmetry described in this paper preserves these capabilities but they are not described in this paper both in order to simplify notation and because the examples of Section VIII do not require these capabilities.

III. SYMMETRIC STATISTICS

The relevant symmetries are the 3-D rotational point group symmetries, which are the icosahedral I , octahedral O , tetrahedral T , cyclic C_n ($n \in \{1, 2, \dots\}$), and dihedral D_n ($n \in \{1, 2, \dots\}$) groups. Once a coordinate system is chosen, each of these groups can be described as a collection of matrices, denoted by $R_\beta \in \mathbb{R}^{3 \times 3}$ ($\beta \in \{1, \dots, N_g\}$), which are rotation matrices, i.e., $R_\beta^{-1} = R_\beta^T$ and $\det R_\beta = +1$. The value of N_g is 60, 24, 12, n , and $2n$ for I , O , T , C_n , and D_n , respectively.

The symmetry can be applied in three different ways. (i) Assume that the particles in a class are identical and that the common electron scattering intensity, which is denoted by $\rho(\mathbf{x})$, has the symmetry, i.e., $\rho(R_\beta^{-1} \mathbf{x}) = \rho(\mathbf{x})$ for all $\beta \in \{1, \dots, N_g\}$ and $\mathbf{x} \in \mathbb{R}^3$. Algorithms and software

for computing structures in this situation are widely available (Section I-A). (ii) Assume that each particle in a class is different but that each particle has the symmetry so that the electron scattering intensity of the i th particle, which is denoted by $\rho_i(\mathbf{x})$, satisfies $\rho_i(R_\beta^{-1}\mathbf{x}) = \rho_i(\mathbf{x})$ for all $\beta \in \{1, \dots, N_g\}$ and $\mathbf{x} \in \mathbb{R}^3$. Algorithms and software for computing structures in this situation are available (Section I-A), but produce anomalous results when symmetry is present [20, p. 173]. (iii) Assume that each particle in a class is different, that no particle has the symmetry, but the statistics of the i.i.d. ensemble of particles has the symmetry as is described in the following paragraph. The authors are unaware of prior work of this type.

One approach to introduce symmetric statistics is to require symmetry in all of the finite-dimensional probability measures that together, via Kolmogorov's extension theorem [54, Theorem 2.1.5 p. 11], define the electron scattering intensity stochastic process. If the probability measures can be described by pdfs, then the symmetry condition is $p_{R_\beta^{-1}\mathbf{x}_1, \dots, R_\beta^{-1}\mathbf{x}_k}(\rho_1, \dots, \rho_k) = p_{\mathbf{x}_1, \dots, \mathbf{x}_k}(\rho_1, \dots, \rho_k)$ for all $\beta \in \{1, \dots, N_g\}$, $k \in \{1, 2, \dots\}$, $\mathbf{x}_1, \dots, \mathbf{x}_k \in \mathbb{R}^3$, and $\rho_1, \dots, \rho_k \in \mathbb{R}$. Define the mean function and covariance function of the electron scattering intensity, denoted by $\bar{\rho}(\mathbf{x})$ and $C(\mathbf{x}_1, \mathbf{x}_2)$, respectively, by $\bar{\rho}(\mathbf{x}) = \mathbb{E}[\rho(\mathbf{x})]$ and $C(\mathbf{x}_1, \mathbf{x}_2) = \mathbb{E}[(\rho(\mathbf{x}_1) - \bar{\rho}(\mathbf{x}_1))(\rho(\mathbf{x}_2) - \bar{\rho}(\mathbf{x}_2))]$, respectively. From the $k = 1$ and $k = 2$ instances of the symmetry condition for the pdfs, it is straightforward to compute that for all $\mathbf{x}, \mathbf{x}_1, \mathbf{x}_2 \in \mathbb{R}^3$ and $\beta \in \{1, \dots, N_g\}$,

$$\bar{\rho}(R_\beta^{-1}\mathbf{x}) = \bar{\rho}(\mathbf{x}) \quad (6)$$

$$C(R_\beta^{-1}\mathbf{x}_1, R_\beta^{-1}\mathbf{x}_2) = C(\mathbf{x}_1, \mathbf{x}_2). \quad (7)$$

If the probability distribution for the electron scattering intensity is Gaussian then (6)–(7) imply that the symmetry condition for the pdfs is satisfied for all values of k .

IV. DESCRIPTION OF $\rho(\mathbf{x})$: BASIS FUNCTIONS

In order to impose the symmetry conditions of (6) and (7) on the electron scattering intensity $\rho(\mathbf{x})$ when $\rho(\mathbf{x})$ is described by (1), it is helpful for the basis functions $F_\omega(\mathbf{x})$ to have particular properties under rotations which are described in this section. As described in Section I-C, in the remainder of the paper we focus on the icosahedral I group because there exist real irreducible representations (irreps) of the group, the natural coordinate system is spherical coordinates, I is important in the structural biology of viruses, and I is the group in our example. The octahedral O group has parallels with I , there exist real irreps and the natural coordinate system is spherical coordinates, so the discussion of I can be carried over to O with no significant changes. The tetrahedral T , cyclic C_n , and dihedral D_n groups require complex irreps and/or cylindrical coordinates and the necessary results are outlined in Appendices D and E.

Using spherical coordinates, we assume that $F_\omega(\mathbf{x}) = I_\omega(\mathbf{x}/x)\psi_\omega(x)$ where $I_\omega(\mathbf{x}/x)$ is the angular basis function

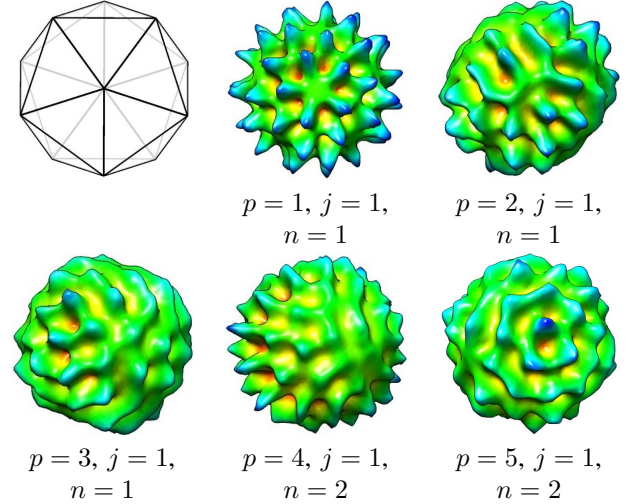


Fig. 1. An icosahedron with a 5-fold axis pointing out of the page and example angular basis functions in the same orientation with $l = 15$ and $p \in \{1, \dots, N_{\text{rep}}\}$. The surfaces of 3-D objects defined by $\xi(\mathbf{x}) = 1$ for $x \leq \kappa_1 + \kappa_2 I_{p,j;l,n}(\mathbf{x}/x)$ and $\xi(\mathbf{x}) = 0$ otherwise, where κ_1 and κ_2 are chosen so that $\kappa_1 + \kappa_2 I_{p,j;l,n}(\mathbf{x}/x)$ varies between 0.5 and 1.0, are visualized by UCSF Chimera [55] where the color indicates the distance from the center of the object. Let $N_E(l)$ denote the number of extreme values (maxima and minima) of $I_{p,j;l,n}(\mathbf{x}/x)$ as \mathbf{x} varies around any great circle grows. The function $N_E(l)$ is a linear function of l with a positive slope. Because $I_{p,j;l,n}(\mathbf{x}/x)$ can be negative, zero, or positive, visualizing $I_{p,j;l,n}(\mathbf{x}/x)$ in the style of this figure requires some transformation of $I_{p,j;l,n}(\mathbf{x}/x)$ and the affine transformation defined by κ_1 and κ_2 is simple.

and is a linear combination of spherical harmonics¹ and $\psi_\omega(x)$ is the radial basis function and is a linear combination of spherical Bessel functions as was used previously [31]. The properties of $F_\omega(\mathbf{x})$ under rotational symmetries involves only $I_\omega(\mathbf{x}/x)$ so $I_\omega(\mathbf{x}/x)$ is the focus of this section.

Ref. [57] derives a basis $I_\omega(\mathbf{x}/x)$ that has particular properties under the operations of a rotational point group. In order to describe the properties of the basis, it is necessary to describe the idea of representations. A representation (rep) of a rotational point group, which is a finite group, is a set of matrices that are homomorphic under matrix multiplication to the group elements [49, p. 61]. The irreducible representations (irreps) of a finite group are a set of unitary reps such that all unitary reps can be decomposed into a direct sum of the irreps [49, Theorem 3.3 p. 69]. As is described in the first paragraph of this section, for I and O , all irreps can be chosen to be real-valued orthonormal rather than complex-valued unitary and this is the situation considered in the remainder of this paper except for Appendices D and E. Let N_{rep} be the number of irreps of the N_g -order group G . Let the set of real-valued matrices in the p th irrep be denoted by $\Gamma^p(g) \in \mathbb{R}^{d_p \times d_p}$ for all $g \in G$ where $p \in \{1, \dots, N_{\text{rep}}\}$. For the icosahedral group, $N_{\text{rep}} = 5$, $N_g = 60$, and $d_p = 1, 3, 3, 4, 5$ for $p = 1, 2, 3, 4, 5$, respectively. The vector-valued basis functions $I_{p,\zeta}(\mathbf{x}/x)$ ($\omega = (p, \zeta)$) were derived [57] by applying real-valued generalized projection

¹Spherical harmonics are denoted by $Y_{l,m}(\theta, \phi)$ where the degree l satisfies $l \in \mathbb{N}$, the order m satisfies $m \in \{-l, \dots, l\}$ and (θ, ϕ) are the angles of spherical coordinates with $0 \leq \theta \leq \pi$ and $0 \leq \phi \leq 2\pi$ [56, Section 14.30, pp. 378–379].

operators, which were constructed from real-valued irreps, to real-valued spherical harmonics. This results in the index ζ being the ordered pair (l, n) , where l indexes the subspace defined by spherical harmonics of degree l , and n indexes the different basis functions within the subspace. The basis functions $I_{p;l,n}(\mathbf{x}/x)$ have the properties

- 1) Each $I_{p;l,n}$ is a d_p -dimensional real-valued vector function, i.e., $I_{p;l,n} \in \mathbb{R}^{d_p}$.
- 2) The $I_{p;l,n}$ functions are orthonormal on the surface of the sphere, i.e.,

$$\int I_{p;l,n}(\mathbf{x}/x) I_{p';l',n'}^T(\mathbf{x}/x) d\Omega = \delta_{p,p'} \delta_{l,l'} \delta_{n,n'} I_{d_p} \quad (8)$$

- 3) The subspace of square integrable functions on the surface of the sphere defined by spherical harmonics of degree l , contains a set of $I_{p;l,n}$ functions with a total of $2l + 1$ components.
- 4) Each $I_{p;l,n}$ function has a specific transformation property under rotations from the rotational point group [58, p. 20], in particular,

$$I_{p;l,n}(R_g^{-1}\mathbf{x}/x) = (\Gamma^p(g))^T I_{p;l,n}(\mathbf{x}/x) \quad (9)$$

where T is transpose and R_g is the 3×3 rotation matrix corresponding to the g th element of the group.

Examples of $I_{p,j;l,n}(\mathbf{x}/x)$ functions for $l = 15$, where $I_{p,j;l,n}(\mathbf{x}/x)$ is the j th component of the d_p -dimensional vector-valued function $I_{p;l,n}(\mathbf{x}/x)$, are visualized in Figure 1. Note, as expected, that the $I_{p=1,j;l,n}(\mathbf{x}/x)$ function exhibits all of the symmetries of an icosahedron since the $p = 1$ irrep is the identity irrep for which $\Gamma^{p=1}(g) = 1$ for all $g \in G$.

V. SYMMETRIC STATISTICS REQUIRES CONSTRAINTS ON THE MOMENTS OF THE WEIGHTS

We use the basis functions of Section IV in (1). Since $\rho(\mathbf{x})$ is real valued and the basis functions are real valued, it is only necessary to consider real-valued weights. We include the radial dependence of the basis function in the weight (which is a vector since the angular basis functions are vector valued) which leads to writing (1) in the form

$$\rho(\mathbf{x}) = \sum_{p=1}^{N_g} \sum_{l=0}^{\infty} \sum_{n=0}^{N_n(p,l)-1} c_{p,\zeta=(l,n)}^T(x) I_{p,\zeta=(l,n)}(\mathbf{x}/x) \quad (10)$$

where $I_{p,\zeta}(\mathbf{x}/x) \in \mathbb{R}^{d_p}$ as in Section IV (p indexes the irrep, ζ is a shorthand for the l and n indices, and d_p is the dimension of the p th irrep), $c_{p,\zeta}(x) \in \mathbb{R}^{d_p}$, and the integer $N_n(p, l)$ (which is the number of basis functions of index l that transform as irrep p) is computed during the computation of $I_{p,\zeta}(\mathbf{x}/x)$. In more detail, the abstract index ω of (1) becomes the triple (p, l, n) and the product $c_\omega F_\omega(\mathbf{x})$ (weight times basis function) of (1) becomes the product $c_{p,\zeta=(l,n)}^T(x) I_{p,\zeta=(l,n)}(\mathbf{x}/x)$. In (30), $c_{p,\zeta=(l,n)}(x)$ is described as a weighted sum of basis functions with weights denoted by $c_{p,\zeta,q}$ and basis functions denoted by $\psi_{p,\zeta,q}(x)$, i.e., $c_{p,\zeta}(x) = \sum_{q=1}^{N_q} c_{p,\zeta,q} \psi_{p,\zeta,q}(x)$. Then c_ω of (1) becomes $c_{p,\zeta,q}$ and $F_\omega(\mathbf{x})$ of (1) becomes $\psi_{p,\zeta,q}(x) I_{p,\zeta=(l,n)}(\mathbf{x}/x)$.

The constraints on the mean function and covariance function of $c_{p,\zeta}(x)$ are derived in Appendices A and B and the

results are stated in this paragraph. The mean obeys the constraint

$$\bar{c}_{p,\zeta}(x) = \begin{cases} \text{arbitrary,} & p \in \{1\} \\ 0_{d_p,1}, & p \in \{2, \dots, N_{\text{rep}}\} \end{cases} \quad (11)$$

The covariance obeys the constraint

$$C_{p_1,\zeta_1;p_2,\zeta_2}(x_1, x_2) = \begin{cases} c_{p_1}(\zeta_1, x_1; \zeta_2, x_2) I_{d_{p_1}}, & p_1 = p_2 \\ 0_{d_{p_1}, d_{p_2}}, & \text{otherwise} \end{cases} \quad (12)$$

where $c_{p_1}(\zeta_1, x_1; \zeta_2, x_2) \in \mathbb{C}$.

The results for the mean function and covariance function of $c_{p,\zeta}(x) \in \mathbb{R}^{d_p}$ given in (11) and (12) are results concerning functions. To reduce these to results concerning finite-dimensional vectors for computation, we assume that $c_{p,\zeta}(x) \in \mathbb{R}^{d_p}$ is described as a linear combination of scalar real-valued orthonormal basis functions with vector real-valued weights. The scalar real-valued orthonormal basis functions are the radial basis functions, denoted by $\psi_\omega(x)$, of Section IV. An exact description would require an infinite number of basis functions but we truncate the number of basis functions to N_q , which sets a limit on the spatial resolution that can be achieved. Based on detailed notation and derivations in Appendix C, the results are

$$\bar{c}_{p,\zeta,q} = \begin{cases} \text{arbitrary,} & p = 1 \\ 0_{d_p,1}, & p \in \{2, \dots, N_{\text{rep}}\} \end{cases} \quad (13)$$

$$\mathbf{V}_{p_1,\zeta_1,q_1;p_2,\zeta_2,q_2} = \begin{cases} v_{p_1}(\zeta_1, q_1; \zeta_2, q_2) I_{d_{p_1}}, & p_1 = p_2 \\ 0_{d_{p_1}, d_{p_2}}, & \text{otherwise} \end{cases} \quad (14)$$

where $v_{p_1}(\zeta_1, q_1; \zeta_2, q_2)$ is arbitrary. The goal of this paper is to estimate $\bar{c}_{p,\zeta,q}$ and $\mathbf{V}_{p_1,\zeta_1,q_1;p_2,\zeta_2,q_2}$ or equivalently $v_{p_1}(\zeta_1, q_1; \zeta_2, q_2)$ from image data.

Equation (14) implies structure for the complete covariance matrix \mathbf{V} . Suppose that the basis functions are enumerated with indices changing in the order p (slowest), ζ , q , and j (fastest) where j is the index that enumerates the elements of the vector $I_{p,\zeta}(\mathbf{x}/x)$. Then the \mathbf{V} matrix is a $N_{\text{rep}} \times N_{\text{rep}}$ block matrix where the size of the blocks is determined by the values of the p indices and only the diagonal blocks are nonzero (due to the “ $p_1 = p_2$ ” condition in (14)). Furthermore, each block is constructed of $N_{\zeta,q} \times N_{\zeta,q}$ subblocks (where $N_{\zeta,q}$ is the total number of (ζ, q) pairs) and each subblock is proportional to the $d_p \times d_p$ identity matrix with proportionality constant $v_{p_1}(\zeta_1, q_1; \zeta_2, q_2)$.

VI. MAXIMUM LIKELIHOOD RECONSTRUCTION WITH SYMMETRIC STATISTICS

The estimator of Section II can be applied to any set of basis functions $F_\omega(\mathbf{x})$, has no constraints on the mean of the coefficients \bar{c} , and has only a positive-definite constraint on the covariance of the coefficients \mathbf{V} . In this section, we specialize to the basis functions of Section IV and add the constraints of Section V on the statistics \bar{c} and \mathbf{V} of the coefficients.

In order to incorporate the basis functions of Section IV and the constraints into the estimator of Section II, we think of the mean vector \bar{c} and covariance matrix \mathbf{V} as functions of a further level of parameterization [59]. In particular: (i) The mean is $\bar{c}(\mu)$ where μ is the arbitrary mean for the $p = 1$ basis

functions since the $p \in \{2, \dots, N_g\}$ basis functions all have zero mean (see (13)). (ii) The covariance is $\mathbf{V}(\mathbf{v})$ where \mathbf{v} is composed of the values $v_{p1}(\zeta_1, q_1; \zeta_2, q_2)$ that are arbitrary except for the requirement that $\mathbf{V}(\mathbf{v})$ be positive definite (see (14)). Using the additional level of parameterization, the gradient and Hessian can be computed via the chain rule. These equations compute the necessary gradient and Hessian in terms of larger vectors and matrices that are then reduced in size. While this approach fits well within the MATLAB software used in Refs. [33]–[38], more efficient approaches may be possible.

We use “Hetero” to indicate the ideas, algorithms, and software of this paper. They are a generalization of Ref. [34] so we use “Hetero (SymPart)” to indicate Ref. [34] and “Hetero (SymStat)” to indicate the generalization. In “Hetero (SymPart)” the particles are heterogeneous and each particle has the symmetry (use $p = 1$ only) while in “Hetero (SymStat)” the particles are heterogeneous, no particle has the symmetry, but the statistics of the particles have the symmetry (use $p \in \{1, \dots, N_{\text{rep}}\}$). Absence of symmetry is a symmetry with just one symmetry operator, the identity operator, and the ideas, algorithms, and software include this case, which we denote by “Hetero (Asymmetry),” since the Hetero (SymPart) and Hetero (SymStat) ideas are identical in the asymmetric case.

The scale of computing for estimators using the three different symmetry assumptions is described in this paragraph in terms of the number of parameters that must be estimated from the data. Figure 2 shows the number of variance parameters that must be estimated (diagonal covariance matrix) as a function of the upper limit on the degree l of the spherical harmonics $Y_{l,m}(\theta, \phi)$ that are included in the mathematical model of the electron scattering intensity. This upper limit is denoted by l_{max} . The number of variance parameters is shown for three cases: (i) Hetero (Asymmetry), (ii) Hetero (SymPart), and (iii) Hetero (SymStat). For both Hetero (SymPart) and Hetero (SymStat), the number of mean parameters is equal to the number of variance parameters for Hetero (SymPart) while for Hetero (Asymmetry) the number of mean parameters equals the number of variance parameters. The curve for the Hetero (Asymmetry) case is exactly $(l_{\text{max}} + 1)^2$ and the other two curves are also approximately quadratic in l_{max} . The attractive aspect of the computational complexity of the Hetero (SymStat) approach is that the Hetero (SymStat) curve is substantially below the Hetero (Asymmetry) curve even though every electron scattering intensity in the Hetero (SymStat) approach is asymmetrical.

In this paragraph we relate the isotropic resolution goal for the mathematical model, denoted by a distance γ , to l_{max} and N_q (the number of radial basis functions $\psi_{p,\zeta,q}(x)$ (see (30))) by counting zero crossings of $I_{p,\zeta=(l,n)}(\mathbf{x}/x)$ for l_{max} and of $c_{p,\zeta=(l,n)}(x)$ for N_q . The particle has radius R . In order to achieve resolution γ in the radial direction it is certainly necessary to have R/γ zero crossings of $c_{p,\zeta=(l,n)}(x)$ between $x = 0$ and $x = R$ and therefore $N_q = R/\gamma$ is required. In order to achieve resolution γ in the angular directions it is certainly necessary to have $2\pi R/\gamma$ zero crossings of $I_{p,\zeta=(l,n)}(\mathbf{x}/x)$ around any great circle and

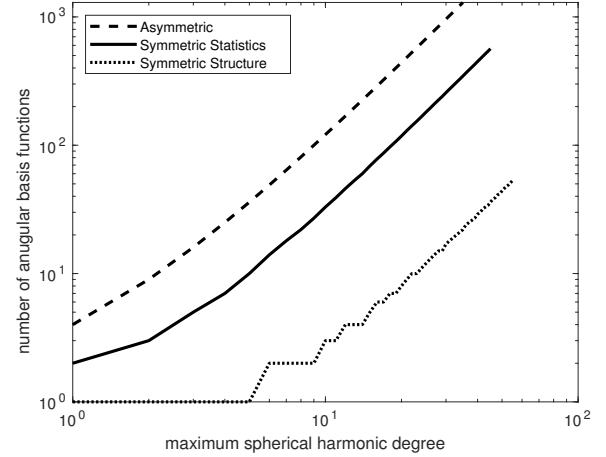


Fig. 2. The number of variance parameters as a function of the maximum degree l_{max} for the three different estimators where two of the estimators incorporate icosahedral symmetry.

therefore $l_{\text{max}} = 2\pi R/\gamma$ is required. The total number of parameters is the number of mean parameters plus the number of variance parameters. For the three different symmetry assumptions described in the previous paragraph, the number of parameters are as follows: Hetero (Asymmetry) requires $(R/\gamma)2\mathcal{K}_{\text{Asym}}(2\pi R/\gamma)$, Hetero (SymPart) requires $(R/\gamma)2\mathcal{K}_{\text{SymPart}}(2\pi R/\gamma)$, and Hetero (SymStat) requires $(R/\gamma)[\mathcal{K}_{\text{SymStat}}(2\pi R/\gamma) + \mathcal{K}_{\text{SymPart}}(2\pi R/\gamma)]$. The values of $\mathcal{K}_{\text{Asym}}(\cdot)$, $\mathcal{K}_{\text{SymStat}}(\cdot)$, and $\mathcal{K}_{\text{SymPart}}(\cdot)$ can be read from Figure 2.

The algorithm has the structure of nested iterations where the inner loop is within MATLAB’s `fmincon`, used to update \mathbf{V} , and the outer loop is the E-M iteration loop. The computational complexity of the algorithm depends on proprietary behavior of `fmincon`, iteration limits, and convergence criteria and so is difficult to quantify. Typically, 8 iterations are used in the inner `fmincon` loop. Typically 20–200 iterations are used in the outer E-M loop depending on the quality of the initial condition. Calculation of $L(z_i)$ for the various values of z_i in the quadrature rule that approximates the integrals in (3)–(5) is the dominant computational cost. The computational complexity of this cost depends on proprietary behavior of MATLAB’s `legendre` function and possibly other functions and so is difficult to quantify. Typically a rule with 5000 abscissas is used. The computational complexity also depends on the number of pixels in an image versus the number of basis functions retained in the truncated orthonormal expansion (i.e., the dimension of $\bar{\mathbf{c}}$) [34, Section 6] since these are the dimensions of the matrix L which occurs throughout the formulas of Section II. Considering just terms in the cost due to the number of images for one iteration of either the inner or the outer loop, these terms are linear in the number of images.

The calculations are performed in three steps. (i) An initial spherically-symmetric reconstruction is estimated from the set of images by using only $l = 0$ basis functions which can be done by least squares. (ii) A homogeneous reconstruction, i.e., a reconstruction in which all particles are assumed to be identical and have icosahedral symmetry, is performed. In terms of Section VI, this is the case where $p = 1$, $\mathbf{c}_i = \bar{\mathbf{c}}$, and

$\mathbf{V} = 0_{N_c, N_c}$ so this algorithm is denoted by *Hetero (zero covar)*. (iii) A heterogeneous reconstruction, i.e., a reconstruction in which no particles are the same, is performed using the homogeneous reconstruction $\bar{\mathbf{c}}$ as an initial condition. Two types of heterogeneous reconstruction are computed and contrasted. One type of reconstruction uses only the $p = 1$ basis functions (*Hetero (SymPart)*), so that each instance of the particle has the icosahedral symmetry. The other type of reconstruction uses the full set of $p \in \{1, \dots, N_{\text{rep}} = 5\}$ basis functions with the constraints of Section V (*Hetero (SymStat)*), so that no instance of the particle has the icosahedral symmetry but the first and second order statistics of the electron scattering intensity $\rho(\mathbf{x})$ do have the icosahedral symmetry. The purpose of Steps (i) and (ii) is to provide an initial condition for Step (iii). Various versions of Steps (i) and (ii) have been used, e.g., switch from homogeneous to heterogeneous reconstructions at low resolution and then increase the resolution, without interpretable differences in the final reconstruction but we do not have a theory or comprehensive results that can be presented here. The *Hetero (zero covar)* followed by *Hetero (SymPart)* reconstructions used basis functions with $p = 1$, $l \in \{0, 1, \dots, 55\}$, and $q \in \{1, 2, \dots, 20\}$ (q indexes the radial basis functions $\psi_{p,\zeta,q}(x)$ (see (30)), 1060 total basis functions) while the *Hetero (zero covar)* followed by *Hetero (SymStat)* reconstructions used $p \in \{1, \dots, N_{\text{rep}}\}$, $l \in \{1, 2, \dots, 10\}$, and $q \in \{1, 2, \dots, 20\}$ (2020 total basis functions) where only smaller l values can be used because of the substantially larger number of basis functions that occur when $p \in \{1, \dots, N_{\text{rep}}\}$ versus $p = 1$. Limited by our computer system, only diagonal \mathbf{V} matrices are considered, which is the simplest case of utilizing all basis functions while guaranteeing the assumption of symmetric statistics. Even with a more powerful computer, estimation of full covariance matrices at the scale of 2020×2020 would probably require regularization, perhaps a sparseness regularizer, and would probably not be done with a maximum likelihood estimator [60].

The mean of the electron scattering intensity, $\bar{\rho}(\mathbf{x}) = E[\rho(\mathbf{x})]$, is related to $\bar{\mathbf{c}}$ by (17) and (31) (or Ref. [34, Eq. 16]). In the simpler notation of (1), the result is $\bar{\rho}(\mathbf{x}) = \sum_{\omega \in \Omega} \bar{\mathbf{c}}_{\omega} F_{\omega}(\mathbf{x})$. The covariance of the electron scattering intensity, $C(\mathbf{x}_1, \mathbf{x}_2) = E[(\rho(\mathbf{x}_1) - \bar{\rho}(\mathbf{x}_1))(\rho(\mathbf{x}_2) - \bar{\rho}(\mathbf{x}_2))]$, is related to \mathbf{V} by (24) and (32) (or Ref. [34, Eq. 18]). In the simpler notation of (1), the result is $C(\mathbf{x}_1, \mathbf{x}_2) = \sum_{\omega \in \Omega} \sum_{\omega' \in \Omega'} \mathbf{V}_{\omega, \omega'} F_{\omega}(\mathbf{x}_1) F_{\omega'}(\mathbf{x}_2)$. The MLE provides estimates of $\bar{\mathbf{c}}$ and \mathbf{V} . Using these estimates in the place of the true values gives the estimates of $\bar{\rho}(\mathbf{x})$ and $C(\mathbf{x}_1, \mathbf{x}_2)$ that are used in this paper and these estimates are themselves maximum likelihood estimates [61, Thm. 7.2.10 p. 320]. We often visualize the estimate of the standard deviation function $s(\mathbf{x}) = \sqrt{C(\mathbf{x}, \mathbf{x})}$, which has the same units as $\bar{\rho}(\mathbf{x})$ and is only 3-D instead of 6-D.

All computations described in this paper were performed on a PC with two Intel Xeon microprocessors (E5-2670, 2.60 GHz) each with 8 cores running CentOS release 6.8 of GNU/Linux. The software for this paper is about 10^4 lines of MATLAB, using `parfor` to achieve multi-core parallelism, running on 12 cores of the PC where the limitation of 12 cores

is set by our license not by the structure of the parallelism. Please contact PCD for a copy of the software.

VII. QUANTIFICATION OF PERFORMANCE

A standard measure of resolution in cryo-EM is the Fourier shell correlation (FSC) (Refs. [62, Eq. 2], [63, Eq. 17], [64, p. 879]) between the estimated electron scattering intensities of two independent reconstructions. FSC is defined by (Ref. [65, Eqs. 22–25])

$$\text{FSC}(k) = \frac{\int P_1(\mathbf{k}) P_2^*(\mathbf{k}) d\Omega'}{\sqrt{\left[\int |P_1(\mathbf{k})|^2 d\Omega' \right] \left[\int |P_2(\mathbf{k})|^2 d\Omega' \right]}} \quad (15)$$

where $P_1(\mathbf{k})$ and $P_2(\mathbf{k})$ are the 3-D Fourier transforms of the electron scattering intensities for the two structures and $\mathbf{k} = (k, \theta', \phi')$ in spherical coordinates. In the approach of this paper, the estimate of the electron scattering intensity is the estimate of $\bar{\rho}(\mathbf{x})$. The behavior of the FSC curve is influenced by the energy that is defined by

$$E(k) = \int |P(\mathbf{k})|^2 d\Omega'. \quad (16)$$

The value of k (denoted by k_*) at which the FSC curve first decreases below a threshold is used to describe the level of similarity of the two structures. For instance, when the two structures are computed from disjoint sets of images of the same particle, then the quantity $1/k_*$ is interpreted as an isotropic spatial resolution of the computation. In the calculations of this paper, the two sets of images are processed completely independently. In this paper, the threshold used is 1/2. While it is standard in structural biology to apply FSC to determine the resolution of the structure, there is no standard for measuring resolution of the covariance function $C(\mathbf{x}_1, \mathbf{x}_2)$, variance function $v(\mathbf{x})$, or standard deviation function $s(\mathbf{x})$. In this paper, we will report norms of the difference of \mathbf{V} values.

VIII. RECONSTRUCTION RESULTS

Numerical results based on cryo-EM images of two different particles, the bacteriophage HK97 [66] and the virus $\text{N}\omega\text{V}$ [67], are described in this section. Numerical results on both synthetic and experimental images of a Virus Like Particle (VLP) derived from bacteriophage HK97 [66] are described in detail in Sections VIII-A and VIII-B, respectively. The VLP is essentially the bacteriophage minus the bacteriophage's portal, tail, and genome leaving only the icosahedrally symmetric capsid. HK97 has a complicated lifecycle wherein it first self-assembles in near equilibrium conditions and then undergoes a sequence of essentially irreversible maturation transformations, which result in a robust particle capable of surviving outside of the host cell. One of the first steps of maturation is the digestion by a virally-encoded protease of the so-called δ domain of the 60×7 copies of the capsid peptide that together make up the capsid of the bacteriophage. (The δ domain is roughly the region between radii 93 Å and 193 Å [33], [68] where the outer radius of the particle is 254 Å [69, PDB 3QPR]) The experimental images [68] come from the particle, denoted by $\text{PhI}^{\text{Pro}+}$ [33], that contains a protease that is defective so that the particle is trapped in the

Prohead I step of maturation. The average outer radius of the capsid is 254 Å [69, PDB 3QPR] and the sphere in which the reconstruction is computed has radius 280 Å.

In addition, numerical results on experimental images of the virus NwV [67] are described in detail in Section VIII-C. NwV has a complicated lifecycle wherein it self-assembles in near equilibrium conditions at neutral pH, undergoes a large reduction in diameter when exposed to acidic conditions, and finally undergoes 60×4 self-catalyzed cleavage reactions in the peptide capsid which makes the diameter reduction irreversible. The experimental images [67] come from particles 30 minutes after the pH change. The average outer radius of the capsid is 211 Å [70, PDB 1OHF] and the sphere in which the reconstruction is computed has radius 230 Å.

The mathematical model of Section II has parameters. The radius R_2 of the ball in which the reconstruction is computed can be estimated directly from micrographs. The measurement noise variance Q is estimated by the average over particles of the sample variance in an annulus surrounding the particle. As is described in Section VI, the truncation of the infinite series of (1) can be related to spatial resolution. The truncation is described by l_{\max} (the highest degree of the spherical harmonics that are retained) and N_q (the number of radial basis functions $\psi_{p,\zeta,q}(x)$ (see (30)) that are retained). We have always retained all harmonics with $l \leq l_{\max}$ and $q \leq N_q$ but that is not required. While the formulas of Section VI allow selecting l_{\max} and N_q based on spatial resolution goals, we have generally been forced to select based on limitations of our computer system (Section VI).

The optimization algorithm for computing the maximum likelihood estimator has parameters. We always start with a spherically-symmetric initial condition ($l_{\max} = 0$) for which the estimator can be computed by a linear least squares problem. Spatial resolution is then increased stepwise. We do not have a theory for whether it is better to first achieve high resolution by *Hetero (SymPart)* and then switch to *Hetero (SymStat)* versus achieve high resolution directly with *Hetero (SymStat)* nor a theory for step sizes and are currently experimenting with these parameters. With the computer system described in Section VI, these choices imply approximately one week calculations. For each resolution step, we use the generalized expectation-maximization algorithm (including the integration rule for the expectation and the maximization algorithm for V) described in Ref. [34].

A. Simulated images: motivated by HK97

Simulated 2-D projection images, directly in reciprocal space, were generated from (2). There are multiple sources of information from which \bar{c} could be computed, including from atomic resolution coordinates from x-ray crystallography experiments. However, there are few sources of information from which V could be computed. The values of \bar{c} and V used in the simulation (“ground truth”) come from the *Hetero (SymStat)* reconstruction results from experimental images for HK97 (Section VIII-B). Each of the 1200 images measures 100×100 pixels with a pixel sampling interval of 5.52 Å. The signal to noise ratio (SNR) is the ratio of the square of

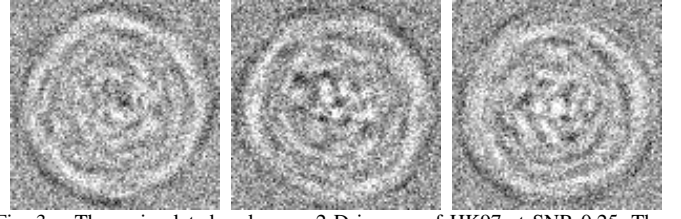


Fig. 3. Three simulated real-space 2-D images of HK97 at SNR 0.25. The color map saturates for the highest 2% of the pixel values.

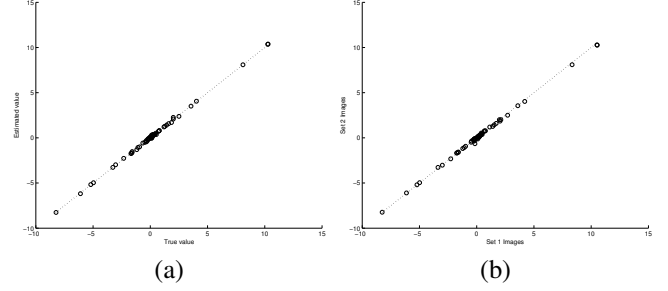


Fig. 4. Scatter plots related to estimates of \bar{c} . (a) True and estimated values of \bar{c} for the synthetic-image calculation of Section VIII-A. (b) Estimated values of the \bar{c} coefficients for two separate *Hetero (SymStat)* calculations starting from separate sets of experimental images (Section VIII-B).

the Euclidean norm of the 100×100 pixel noise-free image to the variance of the additive zero-mean Gaussian noise and has value 0.25. Examples of the simulated real-space 2-D images are shown in Figure 3.

A reconstruction was computed using *Hetero (SymStat)*. Concerning the performance in estimating the mean of the coefficients (\bar{c}), there are only 60 basis functions with $p = 1$ and therefore only 60 coefficients with nonzero mean. A scatter plot of the nonzero coefficients is shown in Figure 4(a). In addition, $\|\hat{c} - c\|_1 / \|c\|_1 = 0.036$ or 3.6%. Concerning the performance in estimating the covariance of the coefficients (V), there are a total of 2020 basis functions and the number of elements in V that can be nonzero is too large to show on a scatter plot. Therefore, we report l_1 norm results: $\|V - \hat{V}\|_1 / \|V\|_1 = 0.12$ or 12%. Resolution is not limited by the amount or the quality of images but rather by the number of Fourier series terms, i.e., number of terms in the summation in (1), that our computer system is capable of processing. The energy curve (16) has decayed by a factor of 10^4 by $k = 0.04$ Å⁻¹ so it is unlikely that resolution is greater than 25 Å.

B. Experimental images: HK97

Limitations of our computer system (Section VI) make it impossible to process the entire set of 5,978 images in Ref. [68] so two sets of 1200 images with no images in common between the two sets and where each image shows one instance of the particle were randomly selected for independent processing. Each image measures 200×200 pixels with a pixel sampling interval of 2.76 Å. Two algorithms, *Hetero (SymPart)* using 1060 basis functions and *Hetero (SymStat)* using 2020 basis functions, were applied to the two sets of images for a total of four reconstructions.

First, consider the *Hetero (SymStat)* results. The same algorithm and parameter values were used in these calcu-

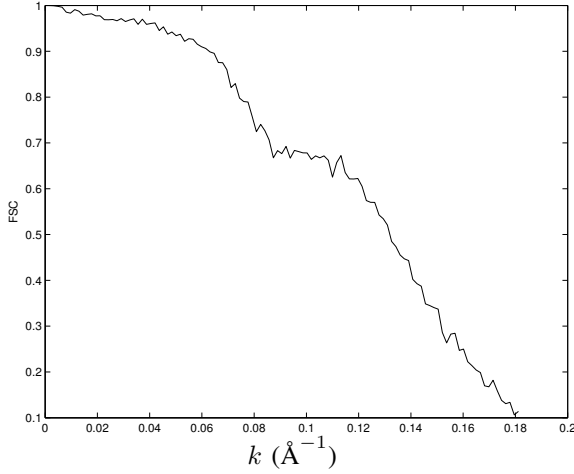


Fig. 5. FSC curve (command `calcfsc` of EMAN2 [8]) comparing two Hetero (*SymPart*) calculations based on separate sets of experimental images using initial conditions derived from the separate sets of images. The resolution (the inverse of the value of k where the curve crosses 0.5) is $1/0.131 = 7.63$ Å.

lations as were used in the synthetic image calculations of Section VIII-A. The results are a scatter plot of non-zero \hat{c}_1 and \hat{c}_2 (Figure 4(b)), $\|\hat{c}_1 - \hat{c}_2\|_1 / (0.5(\|\hat{c}_1\|_1 + \|\hat{c}_2\|_1)) = 0.047$ or 4.7%, and $\|\hat{V}_1 - \hat{V}_2\|_1 / (0.5(\|\hat{V}_1\|_1 + \|\hat{V}_2\|_1)) = 0.10$ or 10%. Resolution is not limited by the amount or the quality of images but rather by the number of coefficients that our computer system is capable of processing. The energy curve (16) has decayed by a factor of 10^4 by $k = 0.04$ Å⁻¹ so it is unlikely that resolution is greater than 25 Å.

Second, consider the Hetero (*SymPart*) results. An FSC curve (command `calcfsc` of EMAN2 [8]) for two estimates of the mean (estimates of $\bar{\rho}(\mathbf{x})$) computed from separate sets of experimental images using initial conditions derived from the separate sets of images is shown in Figure 5. The resolution, which is the inverse of the value of k where the curve crosses 0.5, is $1/0.131 = 7.63$ Å.

Third, compare the Hetero (*SymPart*) and Hetero (*SymStat*) reconstructions. In particular, in Figure 6, the mean $\bar{\rho}(\mathbf{x})$ is visualized for the Hetero (*zero covar*) reconstructions that are Steps (i) and (ii) of the three-step reconstruction process. Furthermore, in Figure 7, the mean $\bar{\rho}(\mathbf{x})$ and the standard deviation $s(\mathbf{x})$ estimates are jointly visualized for both heterogeneous reconstructions by using the $\bar{\rho}(\mathbf{x})$ estimate from Hetero (*SymPart*) to define a shape and the $s(\mathbf{x})$ estimate from either Hetero (*SymPart*) or Hetero (*SymStat*) to color the shape. As is shown in Figure 7(a) (the red radial streaks), Hetero (*SymPart*) estimates a standard deviation function that is organized in radially-organized regions of high standard deviation that lie along all three types of symmetry axis, 2-, 3-, and 5-fold symmetry axes. The highest values are along the 5-fold axes, the lowest along the 2-fold axes, with intermediate values along the 3-fold axes. It is difficult to understand this result in terms of the biology of the particle because the particle is organized in annular shells. In particular, from outside to inside, the Phl^{Pro+} particle is composed of a shell of well-ordered capsid protein, poorly-ordered capsid δ -domain and protease protein, and poorly ordered DNA genome. On the

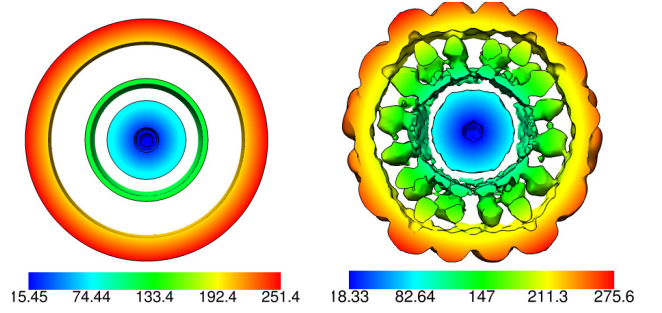


Fig. 6. Visualization of Phl^{Pro+} $\bar{\rho}(\mathbf{x})$ estimates from Hetero (*zero covar*): cross sections of $\bar{\rho}(\mathbf{x})$ estimate (contour level 5×10^{-4}) colored by $\bar{\rho}(\mathbf{x})$ estimate. Left panel: $l = 0$. Right panel: $l = 55$. Both panels: $p = 1$, $q \in \{1, \dots, 20\}$, and $R_2 = 280$ Å. Visualization by UCSF Chimera [55].

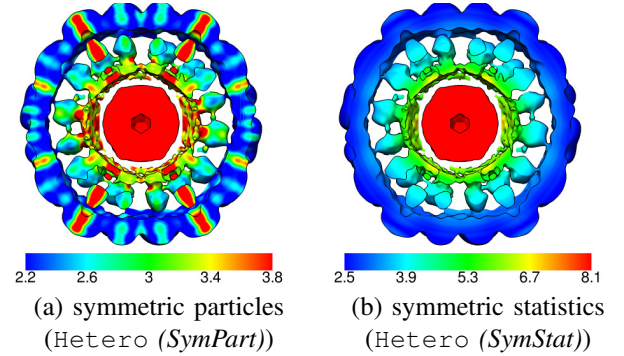


Fig. 7. Joint visualization of $\bar{\rho}(\mathbf{x})$ and $s(\mathbf{x})$ estimates: cross sections of Phl^{Pro+} $\bar{\rho}(\mathbf{x})$ estimate (contour level 5×10^{-4}) from Hetero (*SymPart*) colored by $s(\mathbf{x})$ estimate from Hetero (*SymPart*) (Panel (a)) or Hetero (*SymStat*) (Panel (b)). Panel (a): $p = 1$ and $l \in \{0, 1, \dots, 55\}$. Panel (b): $p \in \{1, \dots, N_{\text{rep}} = 5\}$ and $l \in \{0, 1, \dots, 10\}$. Both panels: $q \in \{1, 2, \dots, 20\}$ and $R_2 = 280$ Å. All markings are scaled by 10^{-3} . Visualization by UCSF Chimera [55].

other hand, Hetero (*SymStat*) estimates a standard deviation function that is organized in annular regions that matches the physical organization of the particle. Using a different approach, specifically, a resampling approach, but still assuming that each instance of the particle is symmetric, this same type of behavior, maxima in the neighborhood of symmetry axes, is well-known to be a common anomalous result [20, p. 173] from standard software systems, e.g., EMAN2 [8]. Our results with Hetero (*SymStat*) suggest a possible solution to this problem. Specifically, if each reconstruction from the resampled data was computed with no symmetry constraints, then the sample mean and covariance of the reconstructions might have no anomalous maxima and (at least approximately) show the symmetry. However, this solution would require a large increase in both computation and data reflecting the difference between the number of variance parameters for a Hetero (*Asymmetry*) calculation versus the number of variance parameters for a Hetero (*SymStat*) calculation in Figure 2.

Finally, in Figure 8, the covariance function of the electron scattering intensity, $C(\mathbf{x}_1, \mathbf{x}_2)$ is visualized for Hetero (*SymStat*) reconstructions of two particles, Phl^{Pro+} and a second particle that entirely lacks the protease which is denoted by Phl^{Pro-}. Phl^{Pro+} and Phl^{Pro-} both trap at the same step in maturation because neither can cleave the capsid protein. To

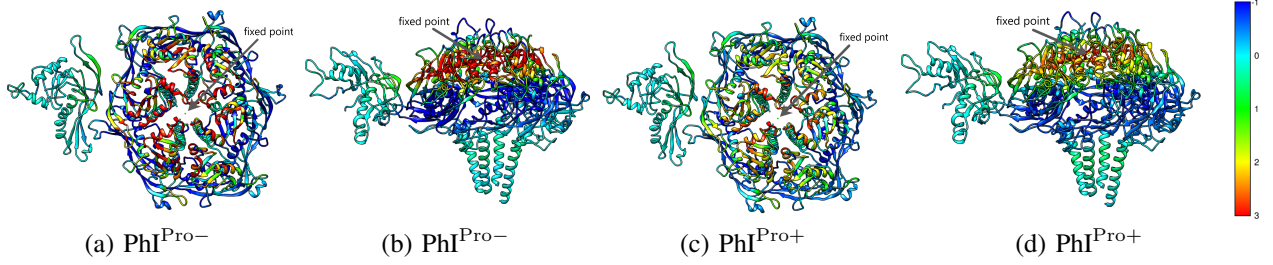


Fig. 8. Visualization of $C(\mathbf{x}_1, \mathbf{x}_2)$ from Hetero (*SymStat*) via ribbon diagrams. Panels (a) and (b): The ribbon diagram showing seven copies of the capsid peptide for $\text{PhiI}^{\text{Pro-}}$ where the color is the value of $C(\mathbf{x}_1, \mathbf{x}_2)$ where \mathbf{x}_2 is fixed at the indicated location while $\mathbf{x}_1 \in \mathbb{R}^3$. Panels (c) and (d): The same as Panels (a) and (b) except for $\text{PhiI}^{\text{Pro+}}$ instead of $\text{PhiI}^{\text{Pro-}}$. Panels (a) and (c): From outside of the particle looking toward the particle's center. Panels (b) and (d): Tangential to the particle's capsid, the external (internal) surface is at the top (bottom) of the image. The protease binds to the δ domain which is the extended alpha helices at the internal surface in the side view. The absence of the protease makes the surface of the capsid rigid. Specifically, $C(\mathbf{x}_1, \mathbf{x}_2 = \mathbf{x}_{\text{fixed}})$ and $\mathbf{x}_{\text{fixed}}$ is on the 5-fold symmetry axis near the external surface of the particle as is indicated by the arrows. If the region of the capsid around $\mathbf{x}_{\text{fixed}}$ is rigid then C will be large, i.e., red, in that region. This is what is seen in $\text{PhiI}^{\text{Pro-}}$, especially the side view of Panel (b). On the other hand, if the region of the capsid around $\mathbf{x}_{\text{fixed}}$ is less rigid then C will be smaller, i.e., yellow, green, ..., down to light blue ($C = 0$) in that region. This is what is seen in $\text{PhiI}^{\text{Pro+}}$, especially the side view of Panel (d), where the region that was mostly red in $\text{PhiI}^{\text{Pro-}}$ is mostly yellow and green in $\text{PhiI}^{\text{Pro+}}$. Since the effect is distant from the binding site of the protease, this is an example of an allosteric interaction. There is no corresponding 6-D visualization of Hetero (*SymPart*) because $C(\mathbf{x}_1, \mathbf{x}_2)$ for Hetero (*SymPart*) is periodic and for that reason is not interpretable. The reason that $C(\mathbf{x}_1, \mathbf{x}_2)$ for Hetero (*SymPart*) is periodic is the fact that for Hetero (*SymPart*), all of the basis functions in (24) are invariant under all of the symmetries of the icosahedral rotational point group. Visualization by UCSF Chimera [55]. For $\text{PhiI}^{\text{Pro+}}$ ($\text{PhiI}^{\text{Pro-}}$), 95.91% (73.91%) of the amino acid residues have covariance values that are between the upper and lower bounds of the colorbar. All markings are scaled by 10^{-6} .

the best of our knowledge, this is the first publication which presents a full 6-D covariance function in the presence of symmetry and the visualization and interpretation of 6-D of information is challenging. In the visualization, one of the locations (\mathbf{x}_2) is fixed at the indicated position and the other location (\mathbf{x}_1) is allowed to vary in \mathbb{R}^3 . The resulting 3-D cube is shown as the color of a ribbon diagram showing each of the seven copies of the capsid peptide. The absence of the protease (which is bound in an unknown location on the inner surface of the capsid) makes the surface of the capsid rigid (large covariance values as indicated by the band of red). Since the effect is distant from the binding site of the protease, this is an example of an allosteric interaction.

C. Experimental images: NwV

The calculations are similar to those of Section VIII-B on HK97. Due to limitations of our computer system (Section VI), we again process only 1200 images. The Hetero (*zero covar*) followed by Hetero (*SymPart*) reconstruction is unchanged from Section VIII-B. The Hetero (*zero covar*) followed by Hetero (*SymStat*) demonstrate the ability of the ideas, algorithms, and software to compute reconstructions in a spherical annulus ($50 \text{ \AA} \leq \|\mathbf{x}\| \leq 230 \text{ \AA}$) rather than simply a ball. The range of l and q have been adjusted, as is described in the captions of Figures 9 and 10, so that the resolution is the same as in the larger HK97 reconstruction.

We focus on whether symmetric statistics is a better mathematical model than the more commonly used symmetric particles. The qualitative aspects of Figure 10 for the NwV calculations closely match those of Figure 7 for the HK97 calculations. In both cases, it is difficult to explain the high standard deviation values that occur along the symmetry axes in the Hetero (*SymPart*) (Panel (a)) calculations. On the other hand, in both cases the radial organization of the standard deviation values in the Hetero (*SymStat*) (Panel (b)) matches the known arrangement of the particles' constituents. As was

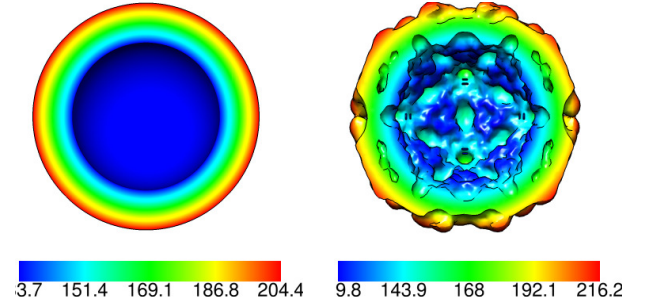


Fig. 9. Visualization of NwV $\bar{\rho}(\mathbf{x})$ estimates from Hetero (*zero covar*): cross sections of $\bar{\rho}(\mathbf{x})$ estimate (contour level 5×10^{-4}) colored by $\bar{\rho}(\mathbf{x})$ estimate. Left panel: $l = 0$. Right panel: $l = 46$. Both panels: $p = 1$, $q \in \{1, \dots, 17\}$, and $R_2 = 230 \text{ \AA}$. This figure is the NwV analog of Figure 6. Visualization by UCSF Chimera [55].

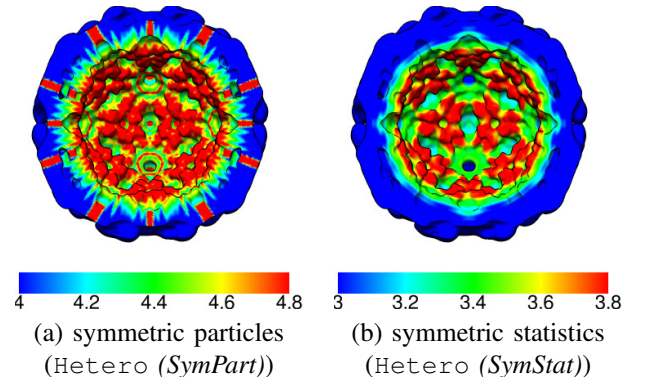


Fig. 10. Joint visualization of $\bar{\rho}(\mathbf{x})$ and $s(\mathbf{x})$ estimates: cross sections of NwV $\bar{\rho}(\mathbf{x})$ estimate (contour level 5×10^{-4}) from Hetero (*SymPart*) colored by $s(\mathbf{x})$ estimate from Hetero (*SymPart*) (Panel (a)) or Hetero (*SymStat*) (Panel (b)). Panel (a): $p = 1$ and $l \in \{0, 1, \dots, 46\}$. Panel (b): $p \in \{1, \dots, N_{\text{rep}} = 5\}$ and $l \in \{0, 1, \dots, 10\}$. Both panels: $q \in \{1, 2, \dots, 17\}$ and $R_2 = 230 \text{ \AA}$. All markings are scaled by 10^{-3} . This figure is the NwV analog of Figure 7. Visualization by UCSF Chimera [55]. In order to better visualize the inner surface of the capsid, a ball of radius 120 \AA containing the genome has been removed. The genome structure varies greatly from particle to particle leading to the high standard deviation values seen on the inner surface of the capsid.

discussed relative to the HK97 calculations, the high standard deviation anomaly is well known [20, p. 173] and these results suggest a possible solution.

IX. CONCLUSION

In this paper we formulate and solve 3-D modeling and reconstruction problems for stochastic signals where the statistics of the stochastic signal are required to have a symmetry. The work is motivated by cryo-electron microscopy, which is of great importance in structural biology and of growing importance in the materials science of nanoscale particles. The focus is on the small-scale heterogeneity that might be characterized for each class of a multi-class reconstruction problem, although the examples described actually are one-class problems.

Previous algorithms assumed that the realizations of the stochastic signal have the symmetry. While this implies that the statistics have the symmetry, it is a sufficient condition rather than a necessary condition and it may be the cause of inaccurate results for the second order statistics of the electron scattering intensity on and near symmetry axes [20, p. 173]. Since symmetry axes are often locations of important biological events, e.g., the 5-fold axis in Flock House Virus (Section I-B), inaccurate results near symmetry axes greatly reduce the value of the entire experiment.

Beyond correcting the problem in existing computations, this is the first publication of which the authors are aware in which a full 6-D covariance function is computed for particles with symmetry. Interpreting the 6-D information is challenging but a simple example concerning allosteric interactions is described in Figure 8. We are working with our biological collaborators to extend these ideas.

APPENDIX A

CONSTRAINT ON THE MEAN FUNCTION OF $c_{p,\zeta}(x)$

Eq. (11) is derived in this section. Define $\bar{\rho}(\mathbf{x}) = \mathbb{E}[\rho(\mathbf{x})] \in \mathbb{R}^1$ and $\bar{c}_{p,\zeta}(x) = \mathbb{E}[c_{p,\zeta}(x)] \in \mathbb{R}^{d_p}$. From (10),

$$\bar{\rho}(\mathbf{x}) = \sum_{p=1}^{N_g} \sum_{\zeta} \bar{c}_{p,\zeta}^T(x) I_{p,\zeta}(\mathbf{x}/x) \quad (17)$$

and from (17) and (9) ($g \in \{1, \dots, N_g\}$)

$$\bar{\rho}(R_g^{-1}\mathbf{x}) = \sum_{p=1}^{N_g} \sum_{\zeta} \bar{c}_{p,\zeta}^T(x) (\Gamma^p(g))^T I_{p,\zeta}(\mathbf{x}/x). \quad (18)$$

From (6) it follows that the left hand sides of (17) and (18) are equal so that for all $g \in \{1, \dots, N_g\}$,

$$\sum_{p=1}^{N_g} \sum_{\zeta} \bar{c}_{p,\zeta}^T(x) [I_{d_p} - (\Gamma^p(g))^T] I_{p,\zeta}(\mathbf{x}/x) = 0. \quad (19)$$

Multiplying by $I_{p',\zeta'}^T(\mathbf{x}/x)$ on the right and integrating over the surface of the sphere implies [via the orthogonality of the $I_{p,\zeta}(\mathbf{x}/x)$ functions (i.e., (8))] that for all $g \in \{1, \dots, N_g\}$,

$$\bar{c}_{p',\zeta'}^T(x) [I_{d_{p'}} - (\Gamma^{p'}(g))^T] = 0_{1,d_{p'}}. \quad (20)$$

Taking transposes and renaming p' to p and ζ' to ζ gives that for all $g \in \{1, \dots, N_g\}$,

$$[I_{d_p} - \Gamma^p(g)] \bar{c}_{p,\zeta}(x) = 0_{d_p,1}. \quad (21)$$

The identity irrep is the $p = 1$ case and for this case, $d_{p=1} = 1$ and $\Gamma^{p=1}(g) = 1$ for all $g \in \{1, \dots, N_g\}$ so that $\bar{c}_{p=1,\zeta}(x)$ is unconstrained by (21). Equation (21) implies that for all $g \in \{1, \dots, N_g\}$,

$$\Gamma^p(g) \bar{c}_{p,\zeta}(x) = \bar{c}_{p,\zeta}(x). \quad (22)$$

Consider $p \in \{2, \dots, N_{\text{rep}}\}$ such that $d_p > 1$. If $\bar{c}_{p,\zeta}(x) \neq 0_{d_p,1}$ then there is at least a one-dimensional subspace that is invariant under the action of $\Gamma^p(g)$ for all $g \in \{1, \dots, N_g\}$ and therefore, by definition [49, p. 67], $\Gamma^p(g)$ is not an irrep. But this contradicts the assumption that $\Gamma^p(g)$ is an irrep. Therefore, the statement $\bar{c}_{p,\zeta}(x) \neq 0_{d_p,1}$ must be false. Finally, consider $p \in \{2, \dots, N_{\text{rep}}\}$ such that $d_p = 1$. If $\bar{c}_{p,\zeta}(x) \neq 0$ then (22) implies that $\Gamma^p(g) = 1$ for all $g \in \{1, \dots, N_g\}$ but this is the identity irrep that is the $p = 1$ irrep. Therefore, $\bar{c}_{p,\zeta}(x) = 0$. These results are summarized in (11).

APPENDIX B

CONSTRAINT ON THE COVARIANCE FUNCTION OF $c_{p,\zeta}(x)$

Eq. (12) is derived in this section acting as if $c_{p,\zeta}(x)$, $I_{p,\zeta}(\mathbf{x}/x)$, and $\Gamma^p(g)$ are complex valued, which simplifies the presentation in Appendix D. Let \mathcal{M}_p be the range of the ordered pair $\zeta = (l, n)$ in the indices of $I_{p,j;l,n}(\mathbf{x}/x)$, which depends on the value of p , e.g., $\zeta, \zeta_1, \zeta_2 \in \mathcal{M}_p$. Define $\bar{\rho}(\mathbf{x}) = \rho(\mathbf{x}) - \bar{\rho}(\mathbf{x})$ and $\tilde{c}_{p,\zeta}(x) = c_{p,\zeta}(x) - \bar{c}_{p,\zeta}$. Define $C(\mathbf{x}_1, \mathbf{x}_2) = \mathbb{E}[(\rho(\mathbf{x}_1) - \bar{\rho}(\mathbf{x}_1))(\rho(\mathbf{x}_2) - \bar{\rho}(\mathbf{x}_2))] = \mathbb{E}[\bar{\rho}(\mathbf{x}_1)\bar{\rho}(\mathbf{x}_2)] \in \mathbb{C}^1$ (as in Section III) and $C_{p_1,\zeta_1;p_2,\zeta_2}(x_1, x_2) = \mathbb{E}[(c_{p_1,\zeta_1}(x_1) - \bar{c}_{p_1,\zeta_1}(x_1))(c_{p_2,\zeta_2}(x_2) - \bar{c}_{p_2,\zeta_2}(x_2))] = \mathbb{E}[\tilde{c}_{p_1,\zeta_1}(x_1)\tilde{c}_{p_2,\zeta_2}^T(x_2)] \in \mathbb{C}^{d_{p_1} \times d_{p_2}}$. Equation (10) implies that

$$\bar{\rho}(\mathbf{x}) = \sum_{p=1}^{N_g} \sum_{\zeta} I_{p,\zeta}^T(\mathbf{x}/x) \tilde{c}_{p,\zeta}(x). \quad (23)$$

From (23) it follows that

$$C(\mathbf{x}_1, \mathbf{x}_2) = \sum_{p_1=1}^{N_{\text{rep}}} \sum_{\zeta_1} \sum_{p_2=1}^{N_{\text{rep}}} \sum_{\zeta_2} I_{p_1,\zeta_1}^T(\mathbf{x}_1/x_1) \times C_{p_1,\zeta_1;p_2,\zeta_2}(x_1, x_2) I_{p_2,\zeta_2}(\mathbf{x}_2/x_2). \quad (24)$$

and from (24) and (9) ($g \in \{1, \dots, N_g\}$) it follows that

$$C(R_g^{-1}\mathbf{x}_1, R_g^{-1}\mathbf{x}_2) = \sum_{p_1=1}^{N_{\text{rep}}} \sum_{\zeta_1} \sum_{p_2=1}^{N_{\text{rep}}} \sum_{\zeta_2} I_{p_1,\zeta_1}^T(\mathbf{x}_1/x_1) \times \Gamma^{p_1}(g) C_{p_1,\zeta_1;p_2,\zeta_2}(x_1, x_2) [\Gamma^{p_2}(g)]^T I_{p_2,\zeta_2}(\mathbf{x}_2/x_2). \quad (25)$$

From (7) it follows that the left hand sides of (24) and (25) are equal so that for all $g \in \{1, \dots, N_g\}$,

$$\sum_{p_1=1}^{N_{\text{rep}}} \sum_{\zeta_1} \sum_{p_2=1}^{N_{\text{rep}}} \sum_{\zeta_2} I_{p_1,\zeta_1}^T(\mathbf{x}_1/x_1) \left[C_{p_1,\zeta_1;p_2,\zeta_2}(x_1, x_2) - \Gamma^{p_1}(g) C_{p_1,\zeta_1;p_2,\zeta_2}(x_1, x_2) [\Gamma^{p_2}(g)]^T \right] I_{p_2,\zeta_2}(\mathbf{x}_2/x_2) = 0. \quad (26)$$

Multiplying on the left by $I_{p'_1, \zeta'_1}^*(\mathbf{x}_1/x_1)$ and on the right by $I_{p'_2, \zeta'_2}^H(\mathbf{x}_2/x_2)$ and integrating over the surface of the sphere for both \mathbf{x}_1 and \mathbf{x}_2 implies [via the orthogonality of the $I_{p, \zeta}(\mathbf{x}/x)$ functions (i.e., (8) with $I_{p', l', n'}^T(\mathbf{x}/x)$ replaced by $I_{p', l', n'}^H(\mathbf{x}/x)$] that for all $g \in \{1, \dots, N_g\}$,

$$C_{p'_1, \zeta'_1; p'_2, \zeta'_2}(x_1, x_2) = \Gamma^{p'_1}(g) C_{p'_1, \zeta'_1; p'_2, \zeta'_2}(x_1, x_2) [\Gamma^{p'_2}(g)]^T. \quad (27)$$

Renaming p'_1, ζ'_1, p'_2 , and ζ'_2 to p_1, ζ_1, p_2 , and ζ_2 , respectively, multiplying on the right by $[\Gamma^{p_2}(g)]^*$, taking advantage of the unitarity of the irrep matrices $\Gamma^p(g)$, and moving the second term to the right hand side of the equation gives

$$C_{p_1, \zeta_1; p_2, \zeta_2}(x_1, x_2) [\Gamma^{p_2}(g)]^* = \Gamma^{p_1}(g) C_{p_1, \zeta_1; p_2, \zeta_2}(x_1, x_2), \quad (28)$$

which must be true for all $g \in \{1, \dots, N_g\}$, $p_1, p_2 \in \{1, \dots, N_{\text{rep}}\}$, $\zeta_1, \zeta_2 \in \mathcal{M}_p$, and $x_1, x_2 \in \mathbb{R}^+ \cup \{0\}$. Finally, use the fact that the irreps $\Gamma^p(g)$ ($p \in \{1, \dots, N_{\text{rep}}\}$, $g \in \{1, \dots, N_g\}$) are real-valued orthonormal rather than complex-valued unitary to get

$$C_{p_1, \zeta_1; p_2, \zeta_2}(x_1, x_2) \Gamma^{p_2}(g) = \Gamma^{p_1}(g) C_{p_1, \zeta_1; p_2, \zeta_2}(x_1, x_2), \quad (29)$$

which must be true for all $g \in \{1, \dots, N_g\}$, $p_1, p_2 \in \{1, \dots, N_{\text{rep}}\}$, $\zeta_1, \zeta_2 \in \mathcal{M}_p$, and $x_1, x_2 \in \mathbb{R}^+ \cup \{0\}$. This set of matrix equations, each of dimension $d_{p_1} \times d_{p_2}$, has substantial structure because the $\Gamma^p(g)$ ($p_1, p_2 \in \{1, \dots, N_{\text{rep}}\}$, $g \in \{1, \dots, N_g\}$) matrices are irreps that are distinct for $p_1 \neq p_2$. Schur's Lemma [49, Corollary 3.2, p. 70] implies (12).

APPENDIX C

$\bar{c}_{p, \zeta, q}$ AND $\mathbf{V}_{p_1, \zeta_1, q_1; p_2, \zeta_2, q_2}$

This section contains detailed notation and derivations for a finite-dimensional description of the mean and covariance of $c_{p, \zeta}(x)$ in terms of the mean vector and covariance matrix of the coefficients in an orthonormal expansion of $c_{p, \zeta}(x)$. The expansion is

$$c_{p, \zeta}(x) = \sum_{q=1}^{N_q} c_{p, \zeta, q} \psi_{p, \zeta, q}(x) \quad (30)$$

where $c_{p, \zeta, q} \in \mathbb{R}^{d_p}$, $\psi_{p, \zeta, q}(x) \in \mathbb{R}$ (the radial basis functions of Section IV), and $\int_{x=0}^{\infty} \psi_{p, \zeta, q_1}(x) \psi_{p, \zeta, q_2}(x) x^2 dx = \delta_{q_1, q_2}$. The goal is to determine the constraints on the mean vector $\bar{c}_{p, \zeta, q}$ and covariance matrix $\mathbf{V}_{p_1, \zeta_1, q_1; p_2, \zeta_2, q_2}$ of the weights $c_{p, \zeta, q}$ where $\bar{c}_{p, \zeta, q} = \mathbb{E}[c_{p, \zeta, q}]$ and $\mathbf{V}_{p_1, \zeta_1, q_1; p_2, \zeta_2, q_2} = \mathbb{E}[(c_{p_1, \zeta_1, q_1} - \bar{c}_{p_1, \zeta_1, q_1})(c_{p_2, \zeta_2, q_2} - \bar{c}_{p_2, \zeta_2, q_2})^T]$. In this notation,

$$\bar{c}_{p, \zeta}(x) = \sum_{q=1}^{N_q} \bar{c}_{p, \zeta, q} \psi_{p, \zeta, q}(x). \quad (31)$$

To determine the mean vector $\bar{c}_{p, \zeta, q}$, substitute (31) into (11), multiply by $\psi_{p, \zeta, q'}(x) x^2$, integrate over $x \in [0, \infty)$, and rename q' to q to find (13).

To determine the covariance matrix $\mathbf{V}_{p_1, \zeta_1, q_1; p_2, \zeta_2, q_2}$, first note from the definition $C_{p_1, \zeta_1; p_2, \zeta_2}(x_1, x_2) = \mathbb{E}[(c_{p_1, \zeta_1}(x_1) - \bar{c}_{p_1, \zeta_1}(x_1))(c_{p_2, \zeta_2}(x_2) - \bar{c}_{p_2, \zeta_2}(x_2))^T]$ that (via (30) and (31))

$$C_{p_1, \zeta_1; p_2, \zeta_2}(x_1, x_2) = \sum_{q_1=1}^{N_q} \sum_{q_2=1}^{N_q} \psi_{p_1, \zeta_1, q_1}(x_1) \times \mathbf{V}_{p_1, \zeta_1, q_1; p_2, \zeta_2, q_2} \psi_{p_2, \zeta_2, q_2}(x_2), \quad (32)$$

so that

$$\mathbf{V}_{p_1, \zeta_1, q'_1; p_2, \zeta_2, q'_2} = \int_{x_1=0}^{\infty} \int_{x_2=0}^{\infty} \psi_{p_1, \zeta_1, q'_1}(x_1) \times C_{p_1, \zeta_1; p_2, \zeta_2}(x_1, x_2) \psi_{p_2, \zeta_2, q'_2}(x_2) x_1^2 x_2^2 dx_1 dx_2. \quad (33)$$

Define $v_{p_1}(\zeta_1, q_1; \zeta_2, q_2) \in \mathbb{R}$ by

$$v_{p_1}(\zeta_1, q_1; \zeta_2, q_2) = \int_{x_1=0}^{\infty} \int_{x_2=0}^{\infty} \psi_{p_1, \zeta_1, q_1}(x_1) \times c_{p_1}(\zeta_1, x_1; \zeta_2, x_2) \psi_{p_1, \zeta_2, q_2}(x_2) x_1^2 x_2^2 dx_1 dx_2. \quad (34)$$

Substitute (12) into the right hand side of (33) and then replace q'_1 and q'_2 by q_1 and q_2 , respectively, to find (14).

APPENDIX D

CASES WHERE REAL-VALUED IRREPS ARE NOT AVAILABLE

Standard references for rotational point group irreps give the irrep matrices in complex-valued unitary form. Frobenius-Schur theory [58, p. 129, Theorem III] implies that among I , O , T , and C_n only for I , O , C_1 , and C_2 does there exist a similarity transformation to a real-valued orthonormal form for all irreps of the group. In this section, the constraints on the moments of the weights caused by symmetric statistics are investigated when the irreps and therefore the basis functions and the weights are complex.

The results for the mean function of $c_{p, \zeta}(x)$ are unaltered from (17)–(22) and (11).

The results for the covariance function of $c_{p, \zeta}(x)$ are changed from (23)–(28). Because the variables are now complex, it is necessary to compute and to apply symmetry constraints to both $C^{p, \rho}(\mathbf{x}_1, \mathbf{x}_2)$ and $C^{p, \rho^*}(\mathbf{x}_1, \mathbf{x}_2)$, which are defined by $C^{p, \rho}(\mathbf{x}_1, \mathbf{x}_2) = \mathbb{E}[(\rho(\mathbf{x}_1) - \bar{\rho}(\mathbf{x}_1))(\rho(\mathbf{x}_2) - \bar{\rho}(\mathbf{x}_2))]$ (the same as $C(\mathbf{x}_1, \mathbf{x}_2)$ in Section V) and $C^{p, \rho^*}(\mathbf{x}_1, \mathbf{x}_2) = \mathbb{E}[(\rho(\mathbf{x}_1) - \bar{\rho}(\mathbf{x}_1))(\rho(\mathbf{x}_2) - \bar{\rho}(\mathbf{x}_2))^*]$, respectively. The calculations for $C^{p, \rho}$ are the same as (23)–(28). In a more detailed notation where $\bar{c}_{p, \zeta}(x) = \mathbb{E}[c_{p, \zeta}(x)]$ and $C_{p_1, \zeta_1; p_2, \zeta_2}^{c, c}(x_1, x_2) = \mathbb{E}[(c_{p_1, \zeta_1}(x_1) - \bar{c}_{p_1, \zeta_1}(x_1))(c_{p_2, \zeta_2}(x_2) - \bar{c}_{p_2, \zeta_2}(x_2))^T]$, the result is

$$C_{p_1, \zeta_1; p_2, \zeta_2}^{c, c}(x_1, x_2) [\Gamma^{p_2}(g)]^* = \Gamma^{p_1}(g) C_{p_1, \zeta_1; p_2, \zeta_2}^{c, c}(x_1, x_2). \quad (35)$$

It is not possible to continue on to (29) because $\Gamma^p(g)$ is no longer real and a new solution is described in the following paragraph. The calculations for C^{p, ρ^*} follow the same plan with the result that $[C_{p_1, \zeta_1; p_2, \zeta_2}^{c, c^*}(x_1, x_2) = \mathbb{E}[(c_{p_1, \zeta_1}(x_1) - \bar{c}_{p_1, \zeta_1}(x_1))(c_{p_2, \zeta_2}^*(x_2) - \bar{c}_{p_2, \zeta_2}^*(x_2))^T]]$

$$C_{p_1, \zeta_1; p_2, \zeta_2}^{c, c^*}(x_1, x_2) \Gamma^{p_2}(g) = \Gamma^{p_1}(g) C_{p_1, \zeta_1; p_2, \zeta_2}^{c, c^*}(x_1, x_2). \quad (36)$$

Equation (36) is of the same form as (29) and so has the same form of solution, which is

$$C_{p_1, \zeta_1; p_2, \zeta_2}^{c, c^*}(x_1, x_2) = \begin{cases} c_{p_1}^{c, c^*}(\zeta_1, x_1; \zeta_2, x_2) I_{d_{p_1}}, & p_1 = p_2 \\ 0_{d_{p_1}, d_{p_2}}, & \text{otherwise} \end{cases} \quad (37)$$

The solution to (35) is described in this paragraph. Two irreps are equivalent [58, Thm. I, p. 71] when there exists an invertible matrix S such that $\Gamma_1(g) = S^{-1}\Gamma_2(g)S$ for all g . Since $\Gamma^{p_2}(g)$ is an irrep, it follows that $[\Gamma^{p_2}(g)]^*$ is a rep. By Ref. [49, Theorem 3.5 p. 70], $[\Gamma^{p_2}(g)]^*$ is an irrep. There is a fixed set of irreps, so there must be a function τ from $\{1, \dots, N_{\text{rep}}\}$ to $\{1, \dots, N_{\text{rep}}\}$ such that $[\Gamma^{p_2}(g)]^* = S^{-1}\Gamma^{\tau(p_2)}(g)S$ for some invertible matrix S . The function τ must be a permutation since if $\tau(p_2) = \tau(p'_2) = p_*$ then $S[\Gamma^{p_2}(g)]^*S^{-1} = \Gamma^{p_*}(g)$ and $S'[\Gamma^{p'_2}(g)]^*[S']^{-1} = \Gamma^{p_*}(g)$. Equating the left hand sides of these two equations gives $S[\Gamma^{p_2}(g)]^*S^{-1} = S'[\Gamma^{p'_2}(g)]^*[S']^{-1}$ which implies $T^{-1}\Gamma^{p_2}(g)T = \Gamma^{p'_2}(g)$ (where $T = [S^{-1}S']^*$) which implies that p_2 and p'_2 are the same irrep. Therefore, (35) is equivalent to

$$C_{p_1, \zeta_1; p_2, \zeta_2}^{c, c}(x_1, x_2) \Gamma^{\tau(p_2)}(g) = \Gamma^{p_1}(g) C_{p_1, \zeta_1; p_2, \zeta_2}^{c, c}(x_1, x_2). \quad (38)$$

Equation (38) is of the same form as (29) and so has the same form of solution, which is

$$C_{p_1, \zeta_1; p_2, \zeta_2}^{c, c}(x_1, x_2) = \begin{cases} c_{p_1}^{c, c}(\zeta_1, x_1; \zeta_2, x_2) I_{d_{p_1}}, & p_1 = \tau(p_2) \\ 0_{d_{p_1}, d_{\tau(p_2)}}, & \text{otherwise} \end{cases} \quad (39)$$

Rather than $C_{p_1, \zeta_1; p_2, \zeta_2}^{c, c}(x_1, x_2)$ and $C_{p_1, \zeta_1; p_2, \zeta_2}^{c, c^*}(x_1, x_2)$, it is probably more natural to work with real-valued functions. This can be achieved by working with the real and imaginary parts of $c_{p, \zeta}(x) - \bar{c}_{p, \zeta}(x)$ leading by standard calculations to formulas for $C_{p_1, \zeta_1; p_2, \zeta_2}^{\Re, \Re}(x_1, x_2)$, $C_{p_1, \zeta_1; p_2, \zeta_2}^{\Re, \Im}(x_1, x_2)$, and $C_{p_1, \zeta_1; p_2, \zeta_2}^{\Im, \Im}(x_1, x_2)$. Either $C_{p_1, \zeta_1; p_2, \zeta_2}^{c, c}(x_1, x_2)$ and $C_{p_1, \zeta_1; p_2, \zeta_2}^{c, c^*}(x_1, x_2)$ or $C_{p_1, \zeta_1; p_2, \zeta_2}^{\Re, \Re}(x_1, x_2)$ and $C_{p_1, \zeta_1; p_2, \zeta_2}^{\Re, \Im}(x_1, x_2)$ can be made finite-dimensional by the same methods used in Section V.

APPENDIX E

USE OF NON-SPHERICAL COORDINATE SYSTEMS

Except in this section, results in this paper are stated in the spherical coordinate system (e.g., (10)). However, for particles obeying the symmetries of C_n (and in some cases D_n) cylindrical coordinates (r, ϕ, z) can be more natural with the single symmetry axis of C_n on the z axis of the coordinate system. For the case of C_n , (10) is replaced by $\rho(\mathbf{x}) = \sum_{p=1}^{N_g} \sum_{\zeta} c_{p, \zeta}^T(r, z) I_{p, \zeta}(\phi)$ and the constraint of symmetric statistics specifies the mean and covariance functions of $c_{p, \zeta}(r, z)$ rather than the mean (see (11)) and covariance (see (12) or (37) and (39)) functions of $c_{p, \zeta}(x)$. In either case, the effect of the symmetric statistics constraint is a constraint on the covariance function of the coordinate-dependent weights where the weights depend on the coordinates that are not involved in the symmetry operation.

ACKNOWLEDGMENTS

We are grateful to Profs. John E. Johnson (The Scripps Research Institute) and David Veesler (Univ. of Washington) for the HK97 data and helpful discussions; to Prof. Johnson and Dr. Tsutomu Matsui (Stanford University) for the NwV data and helpful discussions; to Drs. Yili Zheng, Qiu Wang, and Yunye Gong for their effort on the *Hetero* software; and to NSF 1217867 for support.

REFERENCES

- [1] K. Ma, Y. Gong, T. Aubert, M. Turker, T. Kao, P. C. Doerschuk, and U. Wiesner, "Surfactant micelle self-assembly directed highly symmetric ultrasmall inorganic cages," *Nature*, vol. 558, pp. 577–580, 28 June 2018, <https://doi.org/10.1038/s41586-018-0221-0>.
- [2] G. J. Jensen, Ed., *Cryo-EM, Parts A–C*, ser. Methods in Enzymology. Elsevier Inc., 2010, vol. 481–483.
- [3] S. Subramaniam, W. Kühlbrandt, and R. Henderson, "CryoEM at IUCrJ: a new era," *IUCrJ*, vol. 3, no. 1, pp. 3–7, Jan 2016. [Online]. Available: <https://doi.org/10.1107/S2052252515023738>
- [4] URL, https://www.nobelprize.org/nobel_prizes/chemistry/laureates/2017/advanced-chemistryprize2017.pdf.
- [5] Y. Cheng, "Single-particle cryo-EM—how did it get here and where will it go," *Science*, vol. 361, no. 6405, pp. 876–880, 2018. [Online]. Available: <http://science.sciencemag.org/content/361/6405/876>
- [6] N. Slavov, S. Semrau, E. Airoldi, B. Budnik, and A. van Oudenaarden, "Differential stoichiometry among core ribosomal proteins," *Cell Reports*, vol. 13, pp. 865–873, 3 Nov 2015.
- [7] J. Dubochet, M. Adrian, J.-J. Chang, J.-C. Homo, J. Lepault, A. W. McDowell, and P. Schultz, "Cryo-electron microscopy of vitrified specimens," *Quarterly Reviews of Biophysics*, vol. 21, pp. 129–228, May 1988, <http://dx.doi.org/10.1017/S0033583500004297>.
- [8] G. Tang, L. Peng, P. R. Baldwin, M. D. S., W. Jiang, I. Rees, and S. J. Ludtke, "EMAN2: An extensible image processing suite for electron microscopy," *J. Struct. Biol.*, vol. 157, no. 1, pp. 38–46, 2007.
- [9] S. H. W. Scheres, "RELION: Implementation of a Bayesian approach to cryo-EM structure determination," *J. Struct. Biol.*, vol. 180, no. 3, pp. 519–530, 2012.
- [10] T. R. Shaikh, H. Gao, W. T. Baxter, F. J. Asturias, N. Boisset, A. Leith, and J. Frank, "Spider image processing for single-particle reconstruction of biological macromolecules from electron micrographs," *Nature Protocols*, vol. 3, no. 12, pp. 1941–1974, 2008.
- [11] K. A. Taylor and R. M. Glaeser, "Retrospective on the early development of cryoelectron microscopy of macromolecules and a prospective on opportunities for the future," *J. Struct. Biol.*, vol. 163, pp. 214–223, 2008.
- [12] X.-c. Bai, G. McMullan, and S. H. W. Scheres, "How cryo-EM is revolutionizing structural biology," *Trends in Biochemical Sciences*, vol. 40, no. 1, pp. 49–57, Jan. 2015.
- [13] R. A. Redner and H. F. Walker, "Mixture densities, maximum likelihood and the EM algorithm," *SIAM Review*, vol. 26, no. 2, pp. 195–239, Apr. 1984.
- [14] S. Jonić, "Computational methods for analyzing conformational variability of macromolecular complexes from cryo-electron microscopy images," *Current Opinion in Structural Biology*, vol. 43, pp. 114 – 121, 2017, theory and simulation Macromolecular assemblies. [Online]. Available: <http://www.sciencedirect.com/science/article/pii/S0959440X16302445>
- [15] Q. Jin, C. O. S. Sorzano, J. M. de la Rosa-Trevín, J. R. Bilbao-Castro, R. Núñez Ramírez, O. Llorca, F. Tama, and S. Jonić, "Iterative elastic 3D-to-2D alignment method using normal modes for studying structural dynamics of large macromolecular complexes," *Structure*, vol. 22, no. 3, pp. 496 – 506, 2014. [Online]. Available: <http://www.sciencedirect.com/science/article/pii/S0969212614000136>
- [16] C. O. S. Sorzano, J. M. de la Rosa-Trevín, F. Tama, and S. Jonić, "Hybrid electron microscopy normal mode analysis graphical interface and protocol," *Journal of Structural Biology*, vol. 188, no. 2, pp. 134 – 141, 2014. [Online]. Available: <http://www.sciencedirect.com/science/article/pii/S1047847714001919>

- [17] A. Dashti, P. Schwander, R. Langlois, R. Fung, W. Li, A. Hosseinizadeh, H. Y. Liao, J. Pallesen, G. Sharma, V. A. Stupina, A. E. Simon, J. D. Dinman, J. Frank, and A. Ourmazd, "Trajectories of the ribosome as a brownian nanomachine," *Proceedings of the National Academy of Sciences*, vol. 111, no. 49, pp. 17492–17497, 2014. [Online]. Available: <http://www.pnas.org/content/111/49/17492.abstract>
- [18] J. Frank and A. Ourmazd, "Continuous changes in structure mapped by manifold embedding of single-particle data in cryo-EM," *Methods*, vol. 100, pp. 61–67, 2016. [Online]. Available: <http://www.sciencedirect.com/science/article/pii/S1046202316300251>
- [19] H. D. Tagare, A. Kucukelbir, F. J. Sigworth, H. Wang, and M. Rao, "Directly reconstructing principal components of heterogeneous particles from cryo-EM images," *Journal of Structural Biology*, vol. 191, no. 2, pp. 245–262, 2015. [Online]. Available: <http://www.sciencedirect.com/science/article/pii/S1047847715300046>
- [20] S. J. Ludtke, "Single-particle refinement and variability analysis in EMAN2.1," *Methods in Enzymology*, vol. 579, pp. 159–189, 2016. <http://dx.doi.org/10.1016/bs.mie.2016.05.001>.
- [21] S. H. W. Scheres, "Processing of structurally heterogeneous cryo-EM data in RELION," *Methods in Enzymology*, vol. 579, pp. 125–157, 2016. <http://dx.doi.org/10.1016/bs.mie.2016.04.012>.
- [22] P. A. Penczek, M. Kimmel, and C. M. T. Spahn, "Identifying conformational states of macromolecules by eigen-analysis of resampled cryo-EM images," *Structure*, vol. 19, pp. 1582–1590, 9 November 2011.
- [23] C. M. T. Spahn and P. A. Penczek, "Exploring conformational modes of macromolecular assemblies by multiparticle cryo-EM," *Current Opinion in Structural Biology*, vol. 19, pp. 623–631, 2009.
- [24] W. Zhang, M. Kimmel, C. M. T. Spahn, and P. A. Penczek, "Heterogeneity of large macromolecular complexes revealed by 3D cryo-EM variance analysis," *Structure*, vol. 16, pp. 1770–1776, 2008.
- [25] P. A. Penczek, C. Yang, J. Frank, and C. M. T. Spahn, "Estimation of variance in single-particle reconstruction using the bootstrap technique," *J. Struct. Biol.*, vol. 154, no. 2, pp. 168–183, 2006.
- [26] A. Simonetti, S. Marzi, A. G. Myasnikov, A. Fabbretti, M. Yusupov, C. O. Gualerzi, and B. P. Klaholz, "Structure of the 30S translation initiation complex," *Nature*, vol. 455, no. 7211, pp. 416–420, 18 Sep. 2008. [Online]. Available: <http://dx.doi.org/10.1038/nature07192>
- [27] H. Y. Liao, Y. Hashem, and J. Frank, "Efficient estimation of three-dimensional covariance and its application in the analysis of heterogeneous samples in cryo-electron microscopy," *Structure*, vol. 23, no. 6, pp. 1129–1137, 2 June 2015.
- [28] H. Y. Liao and J. Frank, "Classification by bootstrapping in single particle methods," in *Proceedings of the 2010 IEEE International Symposium on Biomedical Imaging*, 14 Apr. 2010, pp. 169–172.
- [29] E. Katsevich, A. Katsevich, and A. Singer, "Covariance matrix estimation for the cryo-EM heterogeneity problem," *SIAM Imaging Science*, vol. 8, no. 1, pp. 126–185, 2015.
- [30] J. Andén and A. Singer, "Structural variability from noisy tomographic projections," *SIAM Journal on Imaging Sciences*, vol. 11, no. 2, pp. 1441–1492, 2018. [Online]. Available: <https://doi.org/10.1137/17M1153509>
- [31] P. C. Doerschuk and J. E. Johnson, "Ab initio reconstruction and experimental design for cryo electron microscopy," *IEEE Transactions on Information Theory*, vol. 46, no. 5, pp. 1714–1729, Aug. 2000. <http://doi.org/10.1109/18.857786>.
- [32] J. Andén, E. Katsevich, and A. Singer, "Covariance estimation using conjugate gradient for 3d classification in cryo-EM," in *Proceedings of the 2015 IEEE International Symposium on Biomedical Imaging*, 2015, pp. 200–204.
- [33] Y. Gong, D. Veessler, P. C. Doerschuk, and J. E. Johnson, "Effect of the viral protease on the dynamics of bacteriophage HK97 maturation intermediates characterized by variance analysis of cryo EM particle ensembles," *Journal of Structural Biology*, vol. 193, no. 3, pp. 188–195, Mar. 2016. <http://doi.org/10.1016/j.jsb.2015.12.012>.
- [34] Y. Zheng, Q. Wang, and P. C. Doerschuk, "3-D reconstruction of the statistics of heterogeneous objects from a collection of one projection image of each object," *Journal of the Optical Society of America A*, vol. 29, no. 6, pp. 959–970, Jun. 2012. <http://www.doi.org/10.1364/JOSAA.29.000959>.
- [35] Q. Wang, T. Matsui, T. Domitrovic, Y. Zheng, P. C. Doerschuk, and J. E. Johnson, "Dynamics in cryo EM reconstructions visualized with maximum-likelihood derived variance maps," *Journal of Structural Biology*, vol. 181, no. 3, pp. 195–206, Mar. 2013.
- [36] J. Tang, B. M. Kearney, Q. Wang, P. C. Doerschuk, T. S. Baker, and J. E. Johnson, "Dynamic and geometric analyses of *Nudaurelia capensis* ω virus maturation reveal the energy landscape of particle transitions," *Journal of Molecular Recognition*, vol. 27, no. 4, pp. 230–237, 10 February 2014.
- [37] T. Domitrovic, N. Movahed, B. Bothner, T. Matsui, Q. Wang, P. C. Doerschuk, and J. E. Johnson, "Virus assembly and maturation: Auto-regulation through allosteric molecular switches," *Journal of Molecular Biology*, vol. 425, no. 9, pp. 1488–1496, 13 May 2013.
- [38] P. C. Doerschuk, Y. Gong, N. Xu, T. Domitrovic, and J. E. Johnson, "Virus particle dynamics derived from cryoEM studies," *Current Opinion in Virology*, vol. 18, pp. 57–63, 2016. [Online]. Available: <http://dx.doi.org/10.1016/j.coviro.2016.02.011>
- [39] N. Xu, D. Veessler, P. C. Doerschuk, and J. E. Johnson, "Allosteric effects in bacteriophage HK97 procapsids revealed directly from covariance analysis of cryo EM data," *Journal of Structural Biology*, vol. 202, no. 2, pp. 129–141, May 2018. <https://doi.org/10.1016/j.jsb.2017.12.013>. [Online]. Available: <http://www.sciencedirect.com/science/article/pii/S1047847717302368>
- [40] URL, <https://www.rcsb.org/pdb/home/home.do>.
- [41] A. Casañas, J. Querol-Audí, P. Guerra, J. Pous, H. Tanaka, T. Tsukihara, N. Verdager, and I. Fita, "New features of vault architecture and dynamics revealed by novel refinement using the deformable elastic network approach," *Acta Crystallographica Section D*, vol. 69, no. 6, pp. 1054–1061, Jun 2013. [Online]. Available: <https://doi.org/10.1107/S0907444913004472>
- [42] H. Tanaka, K. Kato, E. Yamashita, T. Sumizawa, Y. Zhou, M. Yao, K. Iwasaki, M. Yoshimura, and T. Tsukihara, "The structure of rat liver vault at 3.5 Å resolution," *Science*, vol. 323, no. 5912, pp. 384–388, 2009. [Online]. Available: <http://science.sciencemag.org/content/323/5912/384>
- [43] D. H. Anderson, V. A. Kickhoefer, S. A. Sievers, L. H. Rome, and D. Eisenberg, "Draft crystal structure of the vault shell at 9-Å resolution," *PLOS Biology*, vol. 5, no. 11, pp. 1–10, Nov. 2007. [Online]. Available: <https://doi.org/10.1371/journal.pbio.0050318>
- [44] M. G. Rossmann and J. E. Johnson, "Icosahedral RNA virus structure," *Annual Review of Biochemistry*, vol. 58, no. 1, pp. 533–569, 1989.
- [45] A. J. Fisher and J. E. Johnson, "Ordered duplex RNA controls capsid architecture in an icosahedral animal virus," *Nature*, vol. 361, pp. 176–179, 14 Jan. 1993.
- [46] R. H. Cheng, V. S. Reddy, N. H. Olson, A. J. Fisher, T. S. Baker, and J. E. Johnson, "Functional implications of quasi-equivalence in a $T = 3$ icosahedral animal virus established by cryo-electron microscopy and X-ray crystallography," *Structure*, vol. 2, no. 4, pp. 271–282, 15 Apr. 1994.
- [47] A. Odegard, M. Banerjee, and J. E. Johnson, "Flock House Virus: a model system for understanding non-enveloped virus entry and membrane penetration," *Curr. Top. Microbiol. Immunol.*, vol. 343, pp. 1–22, 2010, doi: 10.1007/82_2010_35; PubMed PMID: 20407886.
- [48] H. E. Walukiewicz, M. Banerjee, A. Schneemann, and J. E. Johnson, "Rescue of maturation-defective Flock House Virus infectivity with noninfectious, mature, viruslike particles," *J. Virol.*, vol. 82, no. 4, pp. 2025–2027, Feb. 2008, PubMed PMID: 18077727; PubMed Central PMCID: PMC2258709.
- [49] W. Miller, Jr., *Symmetry Groups and Their Applications*. San Diego: Academic Press, 1972.
- [50] H. P. Erickson, "The Fourier transform of an electron micrograph—First order and second order theory of image formation," in *Advances in Optical and Electron Microscopy (Volume 5)*, R. Barer and V. E. Cosslett, Eds. London and New York: Academic Press, 1973, pp. 163–199.
- [51] J. Lepault and T. Pitt, "Projected structure of unstained, frozen-hydrated T-layer of *bacillus brevis*," *EMBO J.*, vol. 3, no. 1, pp. 101–105, 1984.
- [52] C. Toyoshima and N. Unwin, "Contrast transfer for frozen-hydrated specimens: Determination from pairs of defocused images," *Ultramicroscopy*, vol. 25, no. 4, pp. 279–291, 1988.
- [53] O. Scherzer, "The theoretical resolution limit of the electron microscope," *J. Appl. Phys.*, vol. 20, pp. 20–29, Jan. 1949.
- [54] B. Øksendal, *Stochastic Differential Equations*, 6th ed. Springer-Verlag, 2003.
- [55] E. F. Pettersen, T. D. Goddard, C. C. Huang, G. S. Couch, D. M. Greenblatt, E. C. Meng, and T. E. Ferrin, "UCSF Chimera—A visualization system for exploratory research and analysis," *J. Comput. Chem.*, vol. 25, no. 13, pp. 1605–1612, 2004.
- [56] F. W. J. Olver, D. W. Lozier, R. F. Boisvert, and C. W. Clark, Eds., *NIST Handbook of Mathematical Functions*. Cambridge, UK: Cambridge University Press, 2010. [Online]. Available: <http://dlmf.nist.gov>
- [57] N. Xu and P. C. Doerschuk, "Computation of real basis functions for the 3-D rotational polyhedral groups T , O , and I ," *In review*, 2017, arXiv:1701.01348.

- [58] J. F. Cornwell, *Group Theory in Physics*. London: Academic Press, 1984, vol. 1.
- [59] N. Xu and P. C. Doerschuk, "Statistical characterization of ensembles of symmetric virus particles: 3-D stochastic signal reconstruction from electron microscope images," in *Proceedings of the 38th Annual International Conference of the IEEE Engineering in Medicine and Biology Society (EMBC'16)*. Orlando, FL: IEEE, 17–20 August 2016, pp. 3977–3980. [Online]. Available: <http://dx.doi.org/10.1109/EMBC.2016.7591598>
- [60] M. Wainwright, R. Tibshirani, and T. Hastie, *Statistical Learning with Sparsity*. CRC Press, 2015.
- [61] G. Casella and R. L. Berger, *Statistical Inference*, 2nd ed. Pacific Grove, CA: Duxbury, Wadsworth Group, 2002.
- [62] M. van Heel, "Similarity measures between images," *Ultramicroscopy*, vol. 21, pp. 95–100, 1987.
- [63] G. Harauz and M. van Heel, "Exact filters for general geometry three dimensional reconstruction," *Optik*, vol. 73, no. 4, pp. 146–156, 1986.
- [64] T. S. Baker, N. H. Olson, and S. D. Fuller, "Adding the third dimension to virus life cycles: Three-dimensional reconstruction of icosahedral viruses from cryo-electron micrographs," *Microbiology and Molecular Biology Reviews*, vol. 63, no. 4, pp. 862–922, Dec. 1999.
- [65] Z. Yin, Y. Zheng, P. C. Doerschuk, P. Natarajan, and J. E. Johnson, "A statistical approach to computer processing of cryo electron microscope images: Virion classification and 3-D reconstruction," *Journal of Structural Biology*, vol. 144, no. 1/2, pp. 24–50, 2003.
- [66] R. W. Hendrix and J. E. Johnson, "Bacteriophage HK97 capsid assembly and maturation," *Exp. Med. Biol.*, vol. 726, pp. 351–363, 2012, doi: 10.1007/978-1-4614-0980-9_15.
- [67] T. Matsui, G. C. Lander, R. Khayat, and J. E. Johnson, "Subunits fold at position-dependent rates during maturation of a eukaryotic RNA virus," *Proceedings of the National Academy of Sciences (USA)*, vol. 107, no. 32, pp. 14 111–14 115, 10 Aug. 2010.
- [68] D. Veelsler, R. Khayat, S. Krishnamurthy, J. Snijder, R. K. Huang, A. J. R. Heck, G. S. Anand, and J. E. Johnson, "Architecture of a dsDNA viral capsid in complex with its maturation protease," *Structure*, vol. 22, pp. 230–237, 2 February 2014. [Online]. Available: <http://dx.doi.org/10.1016/j.str.2013.11.007>
- [69] R. K. Huang, R. Khayat, K. K. Lee, I. Gertsman, R. L. Duda, R. W. Hendrix, and J. E. Johnson, "The Prohead-I structure of bacteriophage HK97: Implications for scaffold-mediated control of particle assembly and maturation," *J. Molecular Biology*, vol. 408, no. 3, pp. 541–554, 6 May 2011.
- [70] C. Helgstrand, S. Munshi, J. E. Johnson, and L. Liljas, "The refined structure of *Nudaurelia capensis* ω Virus reveals control elements for a $T = 4$ capsid maturation," *Virology*, vol. 318, pp. 192–203, 2004.



Peter C. Doerschuk (SM'03) received the B.S., M.S., and Ph.D. degrees in electrical engineering from the Massachusetts Institute of Technology (MIT), Cambridge, in 1977, 1979, and 1985, respectively, and the M.D. degree from Harvard Medical School, Cambridge, MA, in 1987. After postgraduate training at Brigham and Womens' Hospital, he held a postdoctoral appointment with the Laboratory for Information and Decision Systems, MIT, from January 1988 to August 1990. After 16 years on the faculty in Electrical and Computer Engineering, Purdue University, West Lafayette, IN, he joined the faculty in Biomedical Engineering and Electrical and Computer Engineering, Cornell University, Ithaca, NY, in July 2006.



Nan Xu received her Ph.D. degree from the School of Electrical and Computer Engineering with a minor in Applied Mathematics and a minor in Cognitive Neuroscience at Cornell University in May 2017. Nan received her Master of Science degree in May 2015. Before joining Cornell, she received double Bachelor's degrees in Electrical and Computer Engineering (BS) and Mathematics (BA) with a minor in Music at the University of Rochester in Rochester NY. Nan's current research interests are in statistical modeling and inference in biological data.

She is investigating three primary applications: brain network estimation, realistic fMRI data simulation, and reconstruction of the statistical characteristics of ensembles of heterogeneous virus particles.